

# Computation of seismic profiles from mineral physics: the importance of the non-olivine components for explaining the 660 km depth discontinuity

Pierre Vacher <sup>\*,1</sup>, Antoine Mocquet, Christophe Sotin

*UPRES-EA2156 Dynamique et Evolution de la Terre et des Planètes, Laboratoire de Géophysique et Planétologie, Faculté des Sciences et Techniques, 2 rue de la Houssinière, BP 92208, 44322 Nantes Cédex 3, France*

Received 2 December 1996; revised 23 December 1997; accepted 23 December 1997

---

## Abstract

The recent increasing number of experimental works leads us to review the elastic properties and mineralogical transformations of mantle minerals. The updated data set is used to compute seismic profiles for two petrological models along three adiabatic temperature profiles. These profiles are chosen to stress out the influence of non-olivine minerals on seismic parameters, and to represent cold and horizontally averaged temperature profiles of the Earth's mantle. In a first part, starting compositions of pyrolite and piclogite and a single layer convection are assumed. The results clearly point out the importance of the non-olivine part of the mineralogy. Two scenarios are found to explain the 660 km depth discontinuity, whatever the starting composition. (1) Ilmenite appears at the expense of garnet at 660 km depth, and then transforms into perovskite and a small amount of garnet at pressures relevant to the lower mantle (case of a 1500 K adiabat with current phase diagrams). The cumulative effects of the breakdown of  $\gamma$ -spinel and of the reactions involving ilmenite lead to strong seismic discontinuities at 660 km depth followed by relatively small seismic gradients at the top of the lower mantle. (2) Ilmenite is not stable around 660 km depth, and the breakdown of  $\gamma$ -spinel is the only sharp reaction to occur (case of a 1600 K adiabat). Smaller seismic discontinuities are found at 660 km depth, and higher seismic gradients are obtained at the top of the lower mantle. Taking into account experimental uncertainties, the comparison of our calculations with reference seismic models strongly suggests that ilmenite is present at the upper–lower mantle boundary. Along the cold temperature profile (1000 K adiabat), the reactions involving ilmenite appear at separate depths, leading to a complex upper–lower mantle transition with three separate discontinuities. A case with a stratified convection (thermal boundary layer and different compositions between the upper and the lower mantle) is also studied. The strength of the discontinuity induced by the chemical boundary is in a good agreement with seismic observations when a horizontally averaged temperature profile is used for the mantle. This result implies that it is not possible to discriminate between layered or single cell convection in the Earth's mantle. Along the cold temperature profile, the appearance of ilmenite in the upper mantle leads to a second discontinuity in addition to the one imposed by the chemical boundary. Hence, subduction zones should be characterised by a multiple-step transition from the upper to the lower mantle, whatever the chosen style of convection. The proposed

---

<sup>\*</sup> Corresponding author.

<sup>1</sup> Formerly at: Department of Geophysics, Earth Sciences Faculty, Budapestlaan 4, 3508TA Utrecht, The Netherlands.

explanation of the 660 km discontinuity is conformed by recent seismic observations: a complex behaviour of the 660 km discontinuity has indeed been found in subducting slabs, and broadband studies of converted waves have suggested a multiple discontinuities pattern to explain this complexity. © 1998 Elsevier Science B.V. All rights reserved.

**Keywords:** Discontinuity; Mantle; Mineralogy

## 1. Introduction

The seismic discontinuity at 660 km depth is usually explained by the endothermic transition in the olivine system, from  $\gamma$ -spinel to Mg-perovskite + Mg-wüstite. This transition has first been recognised in early studies of the system  $\text{Mg}_2\text{SiO}_4$ – $\text{Fe}_2\text{SiO}_4$  (e.g., Ringwood, 1975; Yagi et al., 1979) and confirmed more recently (e.g., Ito and Takahashi, 1989). Strong arguments in favour of this interpretation arise from seismic observations of the topography of the 660 km depth discontinuity: it is deflected downwards in cold subduction zones, in a good agreement with the endothermic characteristics of the transition (e.g., Revenaugh and Jordan, 1991; Vidale and Benz, 1992; Shearer, 1993; Wicks and Richards, 1993). The attribution of the 660 km depth discontinuity to the transition from  $\gamma$ -spinel to Mg-perovskite + Mg-wüstite has important dynamical consequences. The numerical modelling of mantle convection has shown that the presence of an endothermic phase change stabilises a stratified convection (e.g., Sotin and Parmentier, 1989), except for short periods of ‘avalanches’ in the lower mantle (e.g., Machetel and Weber, 1991; Peltier and Solheim, 1992; Tackley et al., 1994). Such a stratified convection is supported by geochemical arguments (e.g., Allègre and Turcotte, 1986).

It has been proposed that some temperature and/or compositional changes might affect the endothermic character of the transition responsible for the 660 km discontinuity (Liu, 1994; Bina and Liu, 1995). Indeed, olivine and spinel phases account for 40 to 60% of the whole mantle petrology, depending on the petrological model under consideration. The remainder is composed of pyroxene and garnet, for which the high pressure phases, although less well constrained than that of olivine, can show exothermic transitions (e.g., Poirier, 1991; p. 218). The dynamical effect of these variations is to favour a whole mantle convection (Bina and Liu, 1995).

In order to compare quantitatively mineralogical data and seismic observations, it is necessary to compute seismic parameters from thermodynamic theories (e.g., Sammis et al., 1970; Davies and Dziewonski, 1975; Bass and Anderson, 1984; Anderson and Bass, 1986; Duffy and Anderson, 1989; Ita and Stixrude, 1992; Vacher et al., 1996). Unfortunately, the uncertainties on the data which are relevant to mantle minerals are very large, and no consensus has emerged yet in the search of the mineralogy of the mantle using this method: both the classical pyrolite (Ringwood, 1975) and piclogite (Bass and Anderson, 1984) give a good fit to observed seismic models. According to Duffy et al. (1995), comparison of laboratory measurements of the acoustic velocity contrast in the  $\alpha$ -olivine  $\beta$ -spinel system to the magnitude of the seismically observed discontinuity at 410 km depth constrains the olivine content of the upper mantle to be lower than 40 vol%, in contrast with the olivine abundance of the pyrolite model (60%; Ringwood, 1975). Conversely, Ita and Stixrude (1992) concluded that the uppermost mantle must contain 50–60% of olivine, and the lower mantle must be very perovskite-rich (more than 80%) in order to match seismic data (Stixrude et al., 1992; Zhao and Anderson, 1994). In any case, these general trends cannot discriminate between a stratified and a single-layer mantle.

In the present paper, phase equilibria and thermo-elastic data relevant to mantle minerals are reviewed. Then, thermodynamic theories are used to compute density and seismic velocity profiles of the mantle, assuming a whole mantle convection and bulk compositions of pyrolite and piclogite. More attention is put on the region between 600 and 750 km depth, where the non-olivine part of the mineralogy is shown to play an important role. Finally, a case with a chemically and thermally stratified mantle is considered, and the proposed interpretation of the 660 km depth discontinuity is assessed against recent seismological observations.

## 2. Phase equilibria in the mantle

The mineralogy of the mantle is computed as a function of temperature and pressure using the approach developed by Ita and Stixrude (1992, 1993). The phase diagrams of olivine ( $\text{Mg}_{0.89}\text{Fe}_{0.11}\text{SiO}_4$ ) and the remainder ('residuum') are shown in Figs. 1 and 2, respectively. Throughout this paper, the words 'pyrolite' and 'piclogite' will refer to the chemical compositions listed in Table 1. The pyrolite composition is from Irifune (1987); the piclogite composition has been computed in order to get 40% of olivine, and semiequal amount of garnet and pyroxenes (Bass and Anderson, 1984). In agreement with Anderson and Bass (1986), this composition is  $\text{Al}_2\text{O}_3$  rich (8.35 wt.%) compared to pyrolite (5.4 wt.%). Na-rich clinopyroxene is present in pyrolite and absent in piclogite, and Ca-rich garnet is found in piclogite. Since the method used to compute the phase diagrams (Figs. 1 and 2) is extensively described by Ita and Stixrude (1992), together with all the references of experimental works needed to locate the different boundaries, we refer the reader to this latter study. Only a few points relevant to the present study are discussed below.

First, the extent of the olivine +  $\gamma$ -spinel field shown by Ita and Stixrude (1992) is restricted in Fig. 1 to temperatures lower than 1473 K, because no

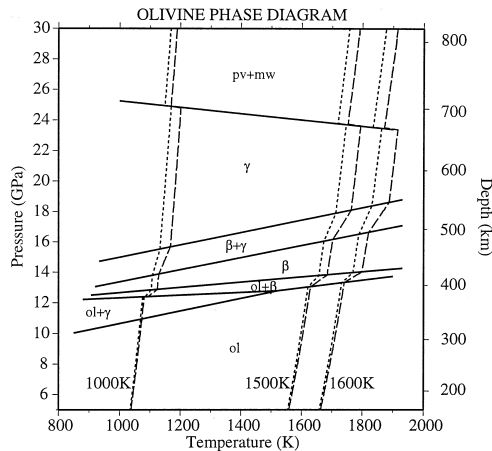


Fig. 1. Phase diagram of olivine ( $\text{Mg}_{0.89}\text{Fe}_{0.11}\text{SiO}_4$ ), modified after Ita and Stixrude (1992). The adiabats initiated at 1000, 1500 and 1600 K are shown for pyrolite (long dashed lines) and piclogite (short dashed lines). ol: olivine;  $\beta$ :  $\beta$ -spinel;  $\gamma$ :  $\gamma$ -spinel; pv: perovskite; mw: Mg-wüstite.

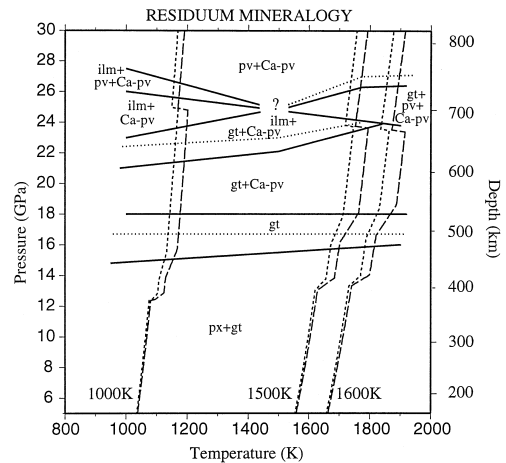


Fig. 2. Mineralogy of the residuum components, after Ita and Stixrude (1992). Solid curves correspond to phase boundaries in a pyrolite composition, dotted curves correspond to phase boundaries in a piclogite composition. The adiabats initiated at 1000, 1500 and 1600 K are shown for pyrolite (long dashed lines) and piclogite (short dashed lines). px: pyroxenes; gt: garnets; Ca-pv: Ca-perovskite; ilm: ilmenite; pv: perovskite.

$\gamma$ -spinel has been observed at higher temperature, neither in the experimental work of Katsura and Ito (1989), nor in the thermodynamic calculations of Akaogi et al. (1989). Note however that this has no effect on the results of Ita and Stixrude (1992), since their study focused on a 1700 K adiabat, which does not cross the olivine +  $\gamma$ -spinel stability field. In their study Ita and Stixrude (1992) took a Clapeyron

Table 1  
Starting compositions

	Pyrolite	Piclogite
<i>Norm, wt. %</i>		
$\text{SiO}_2$	44.31	44.69
$\text{MgO}$	37.82	30.24
$\text{FeO}$	8.56	8.28
$\text{CaO}$	3.48	8.43
$\text{Al}_2\text{O}_3$	5.40	8.35
$\text{Na}_2\text{O}$	0.39	...
<i>Mode, vol %</i>		
Olivine	61.7	40.0
Diopside	13.3	22.0
Enstatite	5.2	8.0
Pyrope	15.3	22.0
Jadeite	4.5	...
Grossular	...	8.0
$\text{FeO/MgO} + \text{FeO}$	0.11	0.11

slope of  $-2.8 \text{ MPa K}^{-1}$  for the breakdown of  $\gamma$ -spinel. Recent values vary between  $-2.0 \text{ MPa K}^{-1}$  (Bina and Helffrich, 1994) and  $-2.8 \text{ MPa K}^{-1}$  (Ito and Takahashi, 1989), with intermediate values of  $-2.5 \text{ MPa K}^{-1}$  (Chopelas et al., 1994), or  $-2.6 \text{ MPa K}^{-1}$  (Akaogi and Ito, 1993). We have tested our results with respect to this parameter, by performing the calculations successively with the two extreme values ( $-2.0 \text{ MPa K}^{-1}$  and  $-2.8 \text{ MPa K}^{-1}$ ). The results did not show any significant variation (except for the location at depth of the breakdown of  $\gamma$ -spinel, which varied by less than 15 km). The value of  $-2.0 \text{ MPa K}^{-1}$  is therefore chosen throughout the paper. Following the experimental work of Wood and Rubie (1996) on the partitioning of Fe and Mg between perovskite and magnesiowüstite in the presence of alumina, we assume an Fe/(Fe + Mg) ratio equal to 0.11 for both phases.

Fig. 2 represents the mineralogy and phase relations in the residuum components; the boundaries drawn with solid lines correspond to a bulk composition of pyrolite, and dotted lines correspond to a bulk composition of piclogite. These latter boundaries are extrapolated using experimental results. Since piclogite is  $\text{Al}_2\text{O}_3$ -rich compared to pyrolite, the different stability fields of ilmenite are reduced in the piclogite phase diagram compared to the pyrolitic one. For the same reason, the stability field of garnet + perovskite at high temperature increases when the  $\text{Al}_2\text{O}_3$  content increases (Kanzaki, 1987; Irifune and Ringwood, 1987; Irifune et al., 1996).

We would like to emphasise here the large uncertainties on the location of the different phase boundaries in Fig. 2, especially around 22–24 GPa. At relatively low temperature (less than 1773 K), the presence of ilmenite, together with garnet at low pressure and perovskite at high pressure, is extensively reported in the literature (e.g., Ito and Navrotsky, 1985; Sawamoto, 1987; Kanzaki, 1987; Irifune and Ringwood, 1987; Kato et al., 1995). At high temperature, experimental studies report the presence of garnet down to the lower mantle, but no ilmenite (e.g., Takahashi and Ito, 1987; O'Neil and Jeanloz, 1994). Furthermore, some recent experiments support the idea that the stability field of garnet in the lower mantle grows up when temperature increases (Irifune, 1994; O'Neil and Jeanloz, 1994). Therefore

we believe that the general topology of the residuum phase diagram as it is shown in Fig. 2 must be a robust feature. But going further into details, important variations in the locations of phase boundaries can exist. As an example, the transition garnet  $\rightarrow$  ilmenite in  $\text{MgSiO}_3$  has been computed by several authors using calorimetric measurements: Fei et al. (1990) and Yusa et al. (1993) found an exothermic transition from garnet to ilmenite, but with different locations, and Saxena et al. (1993) report a Clapeyron slope equal to 0 for this transition. All these calculated phase boundaries are inconsistent with experimentally derived phase diagrams. Reynard and Guyot (1994) and Reynard and Rubie (1996) proposed that these inconsistencies are due to very small intrinsic anharmonic parameters of ilmenite compared to other silicates. Hence the location of the transition garnet  $\rightarrow$  ilmenite, as well as others, is highly uncertain in Fig. 2. Since the junction between relatively high- and low-temperature experiments is highly uncertain, a question mark has been placed for moderate temperatures in Fig. 2. The important feature to our point of view is that the transition from the upper mantle assemblage (pyroxene + garnet) to the lower mantle assemblage (perovskites) depends strongly on temperature, involving ilmenite at low temperatures. All the more detailed features must be regarded with caution.

### 3. Computation of seismic velocities and temperature profiles

The computation of seismic parameters at high temperature and high pressure from mineral physics data has been extensively described in previous papers (e.g., Sammis et al., 1970; Davies and Dziewonski, 1975; Butler and Anderson, 1978; Bass and Anderson, 1984; Duffy and Anderson, 1989; Ita and Stixrude, 1992; Vacher et al., 1996). The calculations at high temperature and high pressure can be performed either simultaneously by applying the Mie–Grüneisen equation of state to thermodynamic potentials (e.g., Stixrude and Bukowinski, 1990; Ita and Stixrude, 1992), or separately, using Grüneisen's and adiabatic finite strain theories (e.g., Duffy and Anderson, 1989; Vacher et al., 1996). The latter solution is used here, with the same formalism as in

Vacher et al. (1996). Here we will only discuss the computation of the temperature profile, and how thermal effects of phase transitions are taken into account.

When calculations at high temperature and high pressure are conducted simultaneously, the derivation of an isentropic temperature profile arises directly from the theory, because the entropy  $S$  derives from the thermodynamic calculations (Ita and Stixrude, 1992). With this method, the thermal effect of phase transitions, or ‘Verhoogen effect’ (Verhoogen, 1965; Jeanloz and Thompson, 1983) is included via the variation of entropy between the different phases. When adiabatic finite strain is used, only the temperature at the foot of the appropriate adiabat is needed for the computation of density and seismic velocities. According to Chopelas and Boehler (1989, 1992), the adiabatic gradient  $(\partial T/\partial P)_S$  can be expressed as

$$\left(\frac{\partial T}{\partial P}\right)_S = \left(\frac{\alpha T}{\rho C_P}\right)_{T,P_0} \left(\frac{\rho_0}{\rho}\right)^{6.5} \quad (1)$$

where  $T$  is temperature,  $P$  is pressure,  $\alpha$  is thermal expansion,  $\rho$  is density,  $C_P$  is heat capacity. The subscript 0 indicates surface conditions. The correction for high pressure involves a power of 6.5 coming from the experimental work of Chopelas and Boehler (1989). The Verhoogen effect of phase transitions can be taken into account by considering different feet of adiabats for the different phases (Vacher et al., 1996). These latter authors have derived a maximum value for the variation of temperature  $\Delta T_{\max}$  at a phase transition:

$$\Delta T_{\max} = \frac{\Gamma T \Delta V}{\bar{C}_P} \quad (2)$$

where  $\Gamma$ ,  $\bar{C}_P$ , and  $\Delta V$  are the Clapeyron slope of the transition, an average heat capacity (Turcotte and Schubert, 1982; p. 193), and the volume change at phase transition, respectively. In the present study, the ‘thermal damping’ due to minerals which are not subject to any phase transition is also taken into account. If  $i$  denotes the minerals subject to a phase transition at a given depth, and  $j$  all the minerals occurring at this depth, a simple energy balance

provides an estimate of the actual temperature variation:

$$\Delta T = \frac{\sum_i \rho_i v_i C_{P_i}}{\sum_j \rho_j v_j C_{P_j}} \Delta T_{\max} \quad (3)$$

where  $v_i$  is the volumetric proportion of the mineral  $i$ . In this study only three phase transitions are considered to generate a significant Verhoogen effect. These are the well-known transitions in the olivine system at approximate depths of 410, 520 and 670 km. The transition from olivine to  $\gamma$ -spinel at low temperature is neglected, since only a small amount of  $\gamma$ -spinel can be created there (less than 10% along the 1000 K adiabat). In the residuum diagram, all the reactions in the pyroxene-garnet solid solution span large ranges of depths and no Verhoogen effect is considered. Figs. 1 and 2 show three adiabatic profiles of pyrolite and piclogite compositions, calculated after Eqs. (1) and (3), with three different feet, namely 1000, 1500 and 1600 K. The motivations in the choice of these three adiabatic profiles are clear in Fig. 2: they cross different series of stability fields around 22–24 GPa, leading to different mineralogical assemblages around the upper–lower mantle transition. The temperature profiles are in a good agreement with the results obtained by Ita and Stixrude (1992) along a warmer adiabat (1700 K), showing warmer profiles and stronger Verhoogen effects for pyrolite than for piclogite. The amplitude of the Verhoogen effect at 670 km depth is of the same order of magnitude than the one obtained by Ita and Stixrude (1992): with a Clapeyron slope equal to  $-2 \text{ MPa K}^{-1}$ , temperature shifts of 45 K and 30 K are obtained along the 1600 K adiabats, for pyrolite and piclogite, respectively. Temperature shifts are equal to 60 K and 40 K for a Clapeyron slope of  $-2.8 \text{ MPa K}^{-1}$ .

Throughout this paper, we use the pressure profile of PREM (Dziewonski and Anderson, 1981).

#### 4. Elasticity data set

Since a few years,  $P$ – $V$ – $T$  measurements with synchrotron-based X-ray diffraction, and sound ve-

locity measurements using opto-acoustic methods have largely increased both the number and accuracy of data relevant to mantle minerals. A compilation of these data is listed in Table 2.

Excellent agreement is found between studies on polycrystalline (e.g., Li et al., 1996) and single-crystal specimens (e.g., Duffy et al., 1995; Zha et al., 1996, 1997) for both  $\alpha$ -olivine and  $\beta$ -spinel. Only the shear modulus of  $\beta$ -spinel shows some variations. For  $\text{Mg}_2\text{SiO}_4$  forsterite, its value ranges from  $G = 108$  GPa (polycrystalline specimen) to  $G = 115$

GPa (single-crystal). The former value is chosen here. We did not put any iron dependence on the bulk moduli for the 3 polymorphs of  $(\text{Mg,Fe})_2\text{SiO}_4$ , following the most recent studies on Fe-bearing samples (e.g., Plymate and Stout, 1994; Abramson et al., 1997). Only selected elastic moduli (e.g.,  $C_{22}$ ) seem to show a systematic variation with composition (Chen et al., 1996).

The considered clinopyroxenes are diopside  $\text{Ca}(\text{Mg,Fe})\text{Si}_2\text{O}_6$ , for which recent compression data are available (Zhang et al., 1997), and jadeite

Table 2  
Elastic parameters of mantle minerals

Mineral	$\rho$ , g cm <sup>-3</sup>	$K_S$ , GPa	$G$ , GPa	$K'_S$	$G'$	$\dot{K}_S$ , GPa K <sup>-1</sup>	$\dot{G}$ , GPa K <sup>-1</sup>
Olivine	3.222	128(1) <sup>a</sup>	81(2) <sup>a,b</sup>	4.3(2) <sup>a</sup>	1.4(3) <sup>a</sup>	-0.016(2) <sup>c</sup>	-0.014(2) <sup>c</sup>
	+ 1.182 $X_{\text{Fe}}$		- 31 $X_{\text{Fe}}$				
$\beta$ -spinel	3.472	170(1) <sup>a</sup>	108(1) <sup>a,d</sup>	4.2(2) <sup>a</sup>	1.5(3) <sup>a</sup>	-0.018(5) <sup>c</sup>	-0.014 <sup>e</sup>
	+ 1.24 $X_{\text{Fe}}$		- 40 $X_{\text{Fe}}$				
$\gamma$ -spinel	3.548	183(3) <sup>f</sup>	119(1) <sup>d</sup>	4.0(3) <sup>f</sup>	1.7(3) <sup>g</sup>	-0.020(3) <sup>f</sup>	-0.014 <sup>e</sup>
	+ 1.30 $X_{\text{Fe}}$		- 40 $X_{\text{Fe}}$				
Diopside (cpx)	3.277	105(1) <sup>h</sup>	67(2) <sup>j</sup>	6.2(3) <sup>h</sup>	1.7 <sup>j</sup>	-0.013 <sup>j</sup>	-0.010 <sup>j</sup>
	+ 0.38 $X_{\text{Fe}}$	+ 13 $X_{\text{Fe}}$	- 6 $X_{\text{Fe}}$	- 1.9 $X_{\text{Fe}}$			
Jadeite (jd)	3.32	126(4) <sup>k</sup>	84(2) <sup>l</sup>	5.0(5) <sup>k</sup>	1.7 <sup>j</sup>	-0.016(5) <sup>k</sup>	-0.013 <sup>j</sup>
Enstatite (opx)	3.215 <sup>m</sup>	124(16) <sup>m</sup>	78 <sup>n</sup>	5.6(29) <sup>m</sup>	1.4(1) <sup>n</sup>	-0.012 <sup>j</sup>	-0.011 <sup>j</sup>
	+ 0.799 $X_{\text{Fe}}$		- 24 $X_{\text{Fe}}$				
Garnet	3.565 <sup>o</sup>	173(2) <sup>o</sup>	92(1) <sup>o</sup>	5.3(2) <sup>p</sup>	2.0(1) <sup>p</sup>	-0.021 <sup>i</sup>	-0.010 <sup>i</sup>
	+ 0.76 $X_{\text{alm}}$	+ 7 $X_{\text{alm}}$	+ 7 $X_{\text{alm}}$				
	- 0.05 $X_{\text{maj}}$	- 10 $X_{\text{maj}}$	- 3 $X_{\text{maj}}$				
Ca-garnet	3.597 <sup>q</sup>	168(1) <sup>q</sup>	107(1) <sup>q</sup>	4.9 <sup>j</sup>	1.6 <sup>j</sup>	-0.015(1) <sup>q</sup>	-0.012(1) <sup>q</sup>
Na-majorite	3.926 <sup>r</sup>	187(2) <sup>r</sup>	115(1) <sup>s</sup>	5.0(5) <sup>r</sup>	1.6 <sup>j</sup>	-0.016 <sup>j</sup>	-0.015 <sup>j</sup>
Mg-perov.	4.108 <sup>t</sup>	264(3) <sup>u</sup>	177(7) <sup>v</sup>	4.0(2) <sup>w</sup>	1.6(2) <sup>x</sup>	-0.015(9) <sup>u</sup>	-0.028(10) <sup>j</sup>
	+ 1.07 $X_{\text{Fe}}$						
Ca-perov.	4.210 <sup>y</sup>	235(8) <sup>y</sup>	150(10) <sup>z</sup>	4.9(3) <sup>y</sup>	1.9 <sup>j</sup>	-0.022(8) <sup>y</sup>	-0.023 <sup>j</sup>
Mg-wüst.	3.584 <sup>aa</sup>	168(2) <sup>aa</sup>	138(2) <sup>aa</sup>	3.6(2) <sup>aa</sup>	1.9(2) <sup>aa</sup>	-0.019(5) <sup>bb</sup>	-0.024(5) <sup>j</sup>
	+ 2.28 $X_{\text{Fe}}$	- 8 $X_{\text{Fe}}$	- 77 $X_{\text{Fe}}$				
Ilmenite	3.810	212(3) <sup>cc</sup>	132(3) <sup>cc</sup>	5.6(10) <sup>dd</sup>	1.7 <sup>j</sup>	-0.017 <sup>j</sup>	-0.017 <sup>j</sup>
	+ 1.1 $X_{\text{Fe}}$		- 41 $X_{\text{Fe}}$				

$\rho$ , density;  $K_S$ , adiabatic bulk modulus;  $G$ , shear modulus;  $K'_S$  and  $G'$ , pressure derivatives of the moduli;  $\dot{K}$  and  $\dot{G}$ , temperature derivatives of the moduli;  $X_{\text{Fe}}$ , mole fraction of iron;  $X_{\text{alm}}$ ,  $X_{\text{maj}}$ , mole fractions of almandine and majorite in garnet solid solution, respectively. Entries in italics are non-experimental values (elasticity systematics). Uncertainties quoted in parentheses apply to the last digit. Except when indicated, densities are after Duffy and Anderson (1989). Sources: (a) Duffy et al. (1995), Li et al. (1996), Zha et al. (1996, 1997); (b) iron dependence after Isaak (1992), Zaug et al. (1993); (c) Isaak (1992), Meng et al. (1993); (d) Weidner et al. (1984); (e) assumed to be identical to  $\alpha$ -olivine values; (f) Meng et al. (1993, 1994); (g) Ridgen et al. (1991); (h) Zhang et al. (1997); (i) Sumino and Anderson (1984); (j) elasticity systematics of Duffy and Anderson (1989); (k) Zhao et al. (1997); (l) Kandelin and Weidner (1988); (m) Angel and Hugh-Jones (1994); iron dependence after Duffy and Anderson (1989); (n) Chai et al. (1997); (o)  $X_{\text{alm}}$  after Chen et al. (1997),  $X_{\text{maj}}$  after Pacalo and Weidner (1997) and Sinogeikin et al. (1997); (p) Ridgen et al. (1994); (q) Isaak et al. (1992); (r) Hazen et al. (1994); (s) Pacalo et al. (1992); (t) Wang et al. (1994); (u) Mao et al. (1991), Lu et al. (1994), Yeganeh-Haeri (1994), Funamori et al. (1996); (v) Yeganeh-Haeri et al. (1989), Weidner et al. (1993), Yeganeh-Haeri (1994); (w) thermodynamic fit to  $P$ - $V$ - $T$  data (Jackson and Ridgen, 1996); (x) elasticity systematics of Zhao and Anderson (1994); (y) Wang et al. (1996); (z) Wolf and Jeanloz (1985); (aa) MgO: computed after the values of Duffy and Ahrens (1995) (see text), iron dependence after Jeanloz and Thompson (1983); (bb) Fei et al. (1992a); (cc) Weidner and Ito (1985); (dd) Reynard et al. (1996). Note the large uncertainties on the temperature derivative of perovskite elastic moduli.

$\text{NaAlSi}_2\text{O}_6$  for which a complete set of thermoelastic equation of state has been reported (Zhao et al., 1997).

(MgFe)SiO<sub>3</sub> pyroxenes show a complex phase diagram: low-clinoenstatite is the stable phase at low  $P$ – $T$  conditions; it transforms to orthoenstatite at temperatures higher than 600°C, and the high pressure phase ( $P > 7$  GPa) is high-clinoenstatite (Woodland and Angel, 1997). The very low-temperature low-clinoenstatite is not considered here, since Angel and Hugh-Jones (1994) have shown that the elastic parameters of ortho- and high-clinoenstatite are indistinguishable within current uncertainties. The adiabatic bulk modulus  $K_S$  of orthoenstatite strongly depends upon  $P$  and  $T$  variations, i.e., the absolute values of its first pressure and temperature derivatives  $K'_S$  and  $\dot{K}_S$ , respectively, are high. Webb and Jackson (1993) and Chai et al. (1997) expressed these characteristics by a quadratic form of the pressure dependence of  $K_S$  (a very high negative second pressure derivative  $K''_S$  compensates for the high positive value of  $K'_S$  at high compression). Angel and Hugh-Jones (1994) proposed a change in the mechanism of compression at pressures close to 4 GPa, and derived two sets of elastic parameters, which are valid for pressures lower, and higher than 4 GPa, respectively. Zhao et al. (1995) gave accurate  $P$ – $V$ – $T$  data for the low pressure orthoenstatite. Since our study focuses on the deepest part of the upper mantle, we only give the properties of the high pressure orthoenstatite ( $P > 4$  GPa; Angel and Hugh-Jones, 1994; Chai et al., 1997). Conversely to this complex behaviour of compressibility, the pressure dependence of the shear modulus has been found to be linear throughout the pressure range (Chai et al., 1997). It has also been suggested that even small substitutions of  $\text{Ca}^{2+}$  and  $\text{Al}^{3+}$  into the pyroxene structure might significantly affect its elasticity (Hugh-Jones and Angel, 1997; Chai et al., 1997), but these effects are not quantitatively measurable yet.

Garnets from complex solid solutions in the Earth's mantle. Recent efforts have been made in order to relate systematic variations of elastic properties, and composition (Hazen et al., 1994; Ridgen et al., 1994; Chen et al., 1997; Pacalo and Weidner, 1997; Sinogeikin et al., 1997). In Table 2, the elastic properties of  $(\text{Mg,Fe})_3\text{Al}_2\text{Si}_3\text{O}_{12}$  solid solutions of

pyrope (Py), almandine (Alm), and majorite (Maj) end-members are listed as variations around the values of the pyrope end-member. Systematics on the pressure derivatives of the isentropic elastic moduli are not yet possible, and we use the data of Ridgen et al. (1994) on  $\text{Py}_{62}\text{Mj}_{38}$  garnet. Ca-garnet (grossular  $\text{Ca}_3\text{Al}_2\text{Si}_3\text{O}_{12}$ ) and Na-majorite are presented separately, because the effects of incorporating  $\text{Ca}^{2+}$  and  $\text{Na}^{2+}$  into the solid solution are unknown at present time. These components are hence treated as independent virtual phases in the present study. At high pressure, jadeite transforms into a Na-majorite structure (Gasparik, 1989) for which experimental values are available (Pacalo et al., 1992; Hazen et al., 1994). We use the value  $K_S = 187$  GPa (Hazen et al., 1994) rather than  $K_S = 173$  GPa (Pacalo et al., 1992), since this latter value comes from a study at ambient conditions, and Na-majorite seems to have a change in compression mechanism at around 2 GPa (see Hazen et al., 1994).

In the lower mantle, perovskites form solid solutions between Mg, Fe, and Al end-members. To our knowledge, no data are available yet for Al-perovskite, and recent compilations (e.g., Ita and Stixrude, 1992) only extrapolate parameters using Mg-perovskite values. Nowadays, a consensus appears concerning the values taken by some of the elastic parameters of  $(\text{Mg,Fe})\text{SiO}_3$  perovskite. The values of  $K_S$  range from 261 GPa to 267 GPa (Mao et al., 1991; Weidner et al., 1993; Yeganeh-Haeri, 1994; Lu et al., 1994), and the value of the pressure derivative is close to 4.0 (Jackson and Ridgen, 1996). However, the values of the thermal parameters, in particular  $\dot{K}_S$  and the thermal expansion  $\alpha$  (Table 3) are still a matter of debate. The measurement of these properties out of the stability field of perovskite may induce biases in the equations of state and in the resulting parameters (Wang et al., 1994; Bina, 1995). We use the equations of state derived by Funamori et al. (1996), yielding  $\dot{K}_S = -0.015 \pm 0.009$  GPa  $\text{K}^{-1}$ , in agreement with the value of Jackson and Ridgen (1996), i.e.,  $\dot{K}_S = -0.011$  GPa  $\text{K}^{-1}$ . Doing so, we follow Anderson (1997) who showed that the previous value  $\dot{K}_S = -0.031$  GPa  $\text{K}^{-1}$  (Stixrude et al., 1992; Zhao and Anderson, 1994) was much too high to get a reasonable Anderson–Grüneisen constant  $\delta_T$ . We also use the parameterisation of Funamori et al. (1996) for thermal

Table 3  
Thermal expansion of mantle minerals

Mineral	a: $10^{-5} \text{ K}^{-1}$	b: $10^{-8} \text{ K}^{-2}$	c: K	d: $10^{-2}$	Refs.
Olivine	2.832	0.758	—	—	Bouhifd et al. (1996)
$\beta$ -spinel	2.711	0.6885	0.5767	—	Fei et al. (1992b)
$\gamma$ -spinel	1.872	0.421	0.6537	—	Meng et al. (1994)
Diopside	3.206	0.811	1.8167	0.1347	Saxena and Shen (1992)
Jadeite	2.56	0.26	—	—	Zhao et al. (1997)
Enstatite	2.86	0.72	—	—	Zhao et al. (1995)
Garnet	2.81	0.316	0.4587	—	Anderson et al. (1991)
Ca-garnet	2.60	0.335	0.6937	—	data from Isaak et al. (1992)
Na-maj.	2.81	0.316	0.4587	—	same as garnet
Mg-pv. <sup>a</sup>	1.913	0.266	0.263	—	$\dot{K}_s = -0.006 \text{ GPa/K}$
	1.982	0.818	0.474	—	$\dot{K}_s = -0.015 \text{ GPa/K}$
	1.933	1.577	0.636	—	$\dot{K}_s = -0.024 \text{ GPa/K}$
Ca-pv.	3.01	0.43	—	—	Wang et al. (1996)
Mg-wüst.	3.681	0.9283	0.7445	—	Fei et al. (1992a)
Ilmenite	2.27	0.682	-0.385	-0.1808	Ashida et al. (1988)

$$\alpha = a + bT - cT^{-2} + dT^{-1}, \alpha \text{ in } \text{K}^{-1}.$$

<sup>a</sup>The three sets of values for Mg-perovskite correspond to the three equations of state (best and extreme fits to  $P$ - $V$ - $T$  data) derived by Funamori et al. (1996). The corresponding values of  $\dot{K}_s$  are given (see Table 2).

expansion, yielding  $\alpha$  (298 K) =  $17 \times 10^{-6} \text{ K}^{-1}$ , a value which is much lower than the value derived by Mao et al. (1991) for experimental reasons detailed in Utsumi et al. (1995). Ca-perovskite is considered as a phase, which appears at a smaller pressure than Mg-perovskite. Values in Tables 2 and 3 come from the study of Wang et al. (1996).

The values given in Table 2 for Mg-wüstite need detailed explanations. Recently, shock-wave experiments have been conducted on a polycrystalline MgO (Duffy and Ahrens, 1995). They found quadratic expressions for the pressure dependence of  $K_s$  and  $G$ , with  $K_s = 162.5 \text{ GPa}$ ,  $K'_s = 4.09$ ,  $K''_s = -0.019 \text{ GPa}^{-1}$ , and  $G = 130.8 \text{ GPa}$ ,  $G' = 2.5$ ,  $G'' = -0.026 \text{ GPa}^{-1}$ . In order to have an internally consistent data base for all mantle minerals, we derived a linear expression of  $K_s$  and  $G$  which is tangent to the quadratic expression in the pressure range of interest (around 670 km depth): the derivatives  $K'_s$  and  $G'$  were computed at a depth of 670 km, and these latter values were used to linearly extrapolate hypothetical values for the moduli at ambient pressure; doing so, we obtained  $K_s = 168 \text{ GPa}$ ,  $K'_s = 3.6$  and  $G = 138 \text{ GPa}$ ,  $G' = 1.9$ . Note that these values have no actual experimental meaning, and are not used outside the pressure range where the linear expression is tangent to the quadratic expression. They are only theoretical

values of the moduli at surface conditions, which fit the shock wave data at pressures relevant to the top of the lower mantle. The temperature dependence of  $K_s$  has been measured by Fei et al. (1992a) on a synthetic crystal ( $\text{Mg}_{0.6}\text{Fe}_{0.4}\text{O}$ ).

Table 2 reveals that the elastic moduli and their pressure derivatives are now experimentally constrained for most of the minerals, conversely to what can be found in previous compilations (e.g., Duffy and Anderson, 1989; Ita and Stixrude, 1992). However, most of the values listed for temperature derivatives do not rely on experiments but on elasticity systematics.

Table 3 gives the thermal expansion  $\alpha$  of minerals in terms of polynomials of temperature. In this compilation, we try to give expressions of  $\alpha(T)$  computed from volume measurements at temperatures relevant to the Earth's mantle. This consideration leads us to provide different forms of polynomials for different minerals. As an example, we refer the reader to the study of Bouhifd et al. (1996) on forsterite. Their measurements up to 2160 K can be fitted by a linear approximation, consistently with the data of Kajiyoishi (1986), and the optimisations of many data by Gillet et al. (1991) and Guyot et al. (1996). Conversely, physically sounded theories can account for the temperature dependence of  $\partial\alpha/\partial T$



(e.g., Skinner, 1966; Suzuki et al., 1984), but they give an overestimated value of thermal expansion at temperatures relevant to the Earth's mantle. In order to compute densities of minerals as a function of  $T$ , we need the integral of  $\alpha$  from 298 K to temperatures relevant to the mantle, rather than  $\alpha(298\text{ K})$ , (e.g., Vacher et al., 1996). Therefore, these considerations are crucial to obtain a better estimation of densities of minerals. In other respects, it is worth keeping in mind that uncertainties on experimental values of thermal expansion are very large; Bouhifd et al. (1996) found uncertainties of the order of 20% of the nominal values of  $\alpha$  for olivine. For Mg-perovskite, three sets of values are given, corresponding to three equations of state, all consistent with  $P$ – $V$ – $T$  data available to date (Funamori et al., 1996). These three expressions of  $\alpha(T)$  must be used consistently with the three respective values of  $\dot{K}_S$  given in Table 2.

## 5. Mineralogical models and seismic profiles of the mantle

Fig. 3 shows the mineralogical models computed from a pyrolite bulk composition, along the three adiabats initiated at 1000, 1500 and 1600 K. As discussed by Bina and Liu (1995) for convection models, the 1000 K adiabat is representative of regions of cold downwellings (subduction zones) and the 1500 and 1600 K adiabats are potential candidates for the horizontally averaged temperature profiles in the mantle. Solid boundaries define the proportions of the different real phases, whereas dashed lines give the proportions of 'virtual' phases, Ca-garnet and Na-majorite, within the garnet solid solution.

The effect of temperature on the olivine part of the mineralogy is very simple, and is only due to the amplitude and sign of the Clapeyron slopes of the transitions: when temperature increases, the fields of  $\alpha$ -olivine and  $\beta$ -spinel expand, whereas the field of  $\gamma$ -spinel narrows. The presence of  $\gamma$ -spinel at shallow depth (around 350 km) in the 1000 K composition is of small importance, since only 6% of  $\gamma$ -spinel appears. We will put more emphasis on the effect of temperature on the residuum part of the mineralogy. Down to 650 km depth, the temperature effect is

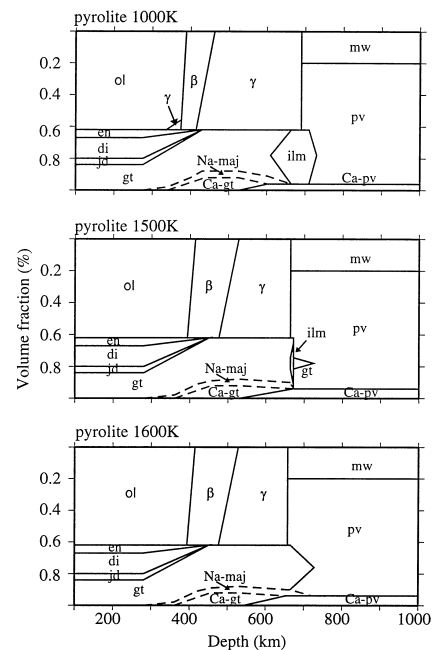


Fig. 3. Volumic proportions of minerals and phases present in the pyrolite composition as a function of depth, along the 1000 K (top) and 1500 K (middle) and 1600 K (bottom) adiabats. Dashed lines give the proportions of 'virtual phases', which are part of the garnet solid solution. en: enstatite; di: diopside; jd: jadeite; Ca-gt: Ca-garnet; Na-maj: Na-majorite; other symbols are defined in Fig. 1 and Fig. 2.

small: when temperature increases, the different substitutions in the garnet solid solution occur at different depths (dissolution of the pyroxenes into a garnet structure, appearance of Ca- and Na-bearing garnets and Ca-perovskite). But temperature has a great effect on the reaction to lower mantle assemblages. At low temperature, garnet disappears into an ilmenite structure at about 620 km depth; this reaction gives rise to a great amount of ilmenite, 32% down to 710 km depth. Then, ilmenite transforms into perovskites, within a 20 km thick layer. Ilmenite is also observed along the 1500 K adiabat, but within a thinner layer (around 8 km thick). Then, a small amount of garnet is present in the lower mantle (7%). The experimental study of the system  $\text{MgSiO}_3$ – $\text{Al}_2\text{O}_3$  has been done by Irifune and Ringwood (1987) and Irifune et al. (1996); for a pyrolitic  $\text{Al}_2\text{O}_3$  content, their phase diagrams show first that the reaction garnet  $\rightarrow$  garnet + ilmenite consumes the most part of the garnet, and second that the reaction

garnet + ilmenite  $\rightarrow$  garnet + perovskite occurs instantaneously (24 GPa at 1500°C). Note that following these reactions, both ilmenite and Mg-perovskite contain a non-negligible amount of alumina. It is not taken into account in the calculations, due to the lack of relevant experimental data. It must be also emphasised that these two transformations in the pyroxene stoichiometry occur near 670 km depth along the 1500 K adiabat. Along the 1600 K adiabat, the stability field of ilmenite is not crossed anymore by the temperature profile; in that case, garnet gradually transforms into a perovskite structure within a binary phase loop. The reaction is completed at a depth of 725 km.

Fig. 4 shows the mineralogical models computed with a starting composition of piclogite. The features previously described for a pyrolitic composition are slightly different in the piclogite case. First, piclogite contains only 40% of olivine, and thus the features found in the residuum part of the mineralogy are amplified; second, piclogite is more  $\text{Al}_2\text{O}_3$ -rich than pyrolite, and this leads to smaller stability fields of ilmenite (Fig. 2). Along the cold temperature profile, the mantle is composed of 42% of ilmenite, between

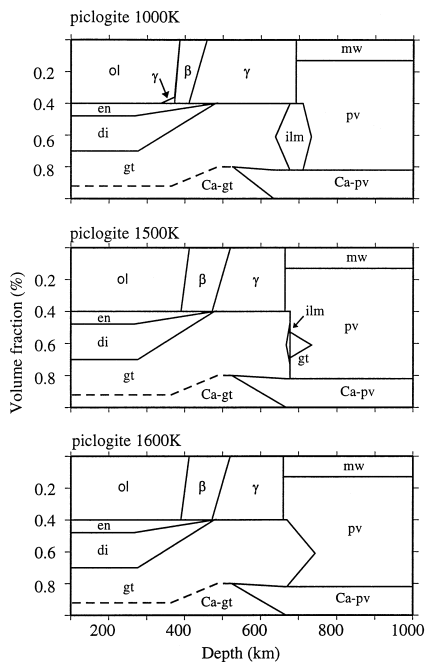


Fig. 4. Same as Fig. 3, for a bulk composition of piclogite.

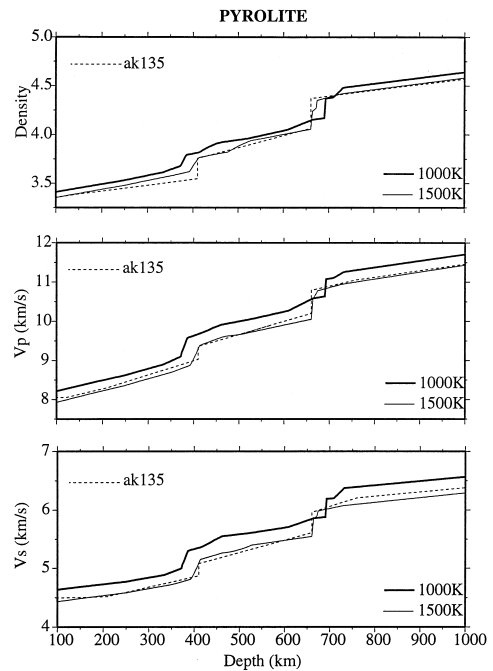


Fig. 5. Synthetic profiles of density (top), P-wave velocity (middle) and S-wave velocity (bottom) as a function of depth, for a pyrolite composition in both upper and lower mantles. Bold (thin) lines correspond to profiles computed along the 1000 K (1500 K) adiabat. Globally averaged seismic model is ak135 (Kennett et al., 1995; dashed lines).

638 km and 710 km depth. Along the 1500 K profile, ilmenite appears at 665 km depth, and forms 29% of the mantle at 677 km depth. Again, it transforms instantaneously into perovskite and garnet, but 16% of garnet are present at 680 km depth. Therefore the increased  $\text{Al}_2\text{O}_3$  content in piclogite diminishes the role of ilmenite: only 29% of ilmenite are formed at 677 km in piclogite, vs. 32% in pyrolite; 16% of garnet are still present at the top of the piclogitic lower mantle, vs. only 7% in the pyrolitic lower mantle. In other words, the short appearance of ilmenite consumes 75% of the garnet content of the pyrolitic mantle, vs. only 60% of the garnet content of the piclogitic mantle.

Figs. 5 and 6 show the profiles of density, P- and S-wave velocities obtained along the 1000 K (bold lines) and 1500 K (thin lines) adiabats, with bulk compositions of pyrolite and piclogite, respectively. Computed profiles are first compared to the ak135 model (Kennett et al., 1995). This latter model was

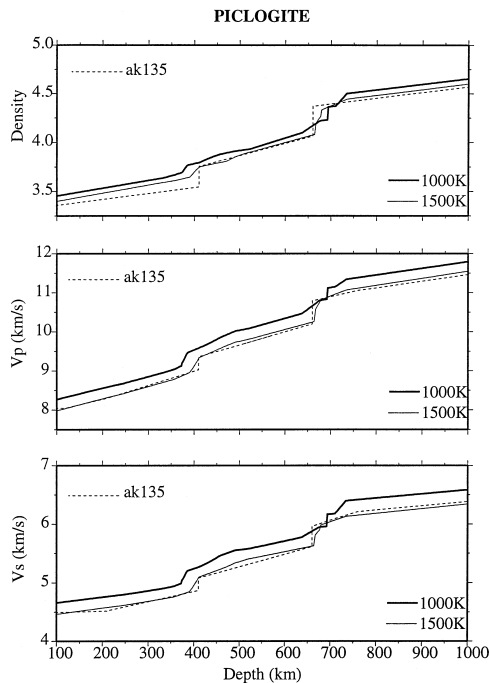


Fig. 6. Same as Fig. 5, for a bulk composition of piclogite.

constructed after travel time data. It is thus adequate for the locations at depth of seismic discontinuities and associated velocity jumps, but does not give access to density directly from the data. Normal mode observations are required for this purpose. In the following, both PREM (Dziewonski and Anderson, 1981) and ak135 (Kennett et al., 1995) will be used as globally averaged seismic models. Montagner and Kennett (1996) have shown that body wave and normal mode globally averaged seismic models could be reconciled by inverting the parameters that cannot be extracted from body-waves, under the constraints of fixed isotropic P- and S-wave velocities. This rigorous approach is not used here. Both PREM and ak135 are used to define a range of variations for seismic parameters.

P- and S-wave velocities computed in the uppermost mantle (100–400 km depth) along the 1500 K adiabat are close to the observed ones, both in gradients and absolute values, whatever the chosen composition. Conversely, density profiles are up to 5% higher than the seismically derived profile for both compositions. One explanation for this density misfit can be the large experimental uncertainties on

values of thermal expansion, mentioned in the previous section. On the basis of these comparisons, it is not possible to discriminate between pyrolite and piclogite. Looking at the amplitude of the 410 km discontinuity, we find, as Duffy et al. (1995) did, that the piclogite composition gives a better match to the 410 discontinuity than pyrolite. This latter composition overestimates the velocity jump by 35% for P-waves and 40% for S-waves.

In the lower mantle (below 750 km depth), all profiles computed along the 1500 K adiabat show synthetic gradients and absolute values of density and seismic velocities in good agreement with observed values. However, we will not give too much importance to this result: recent systematics have clearly shown that, given present-day uncertainties on thermoelastic data, it is not yet possible to estimate the lower mantle chemistry uniquely from seismic data (e.g., Zhao and Anderson, 1994). As an example, we have tested an other partitioning coefficient between perovskite and Mg-wüstite, found in experiments on Al-free systems ( $K_{\text{Mg-Fe}}^{\text{pv-mw}} = 0.4$ , Katsura and Ito, 1996; Martinez et al., 1997). The density and velocity profiles obtained in this way are identical to the ones presented here.

## 6. Characteristics of the 660 km depth discontinuity in globally averaged models

Figs. 7 and 8 show the density, P- and S-wave profiles computed along the 1500 K and 1600 K profiles, between depths of 600 and 750 km, with a bulk composition of pyrolite and piclogite, respectively. PREM (Dziewonski and Anderson, 1981) and ak135 (Kennett et al., 1995) models are shown for comparison, and the different reactions are located along the horizontal axis. The location at depth and amplitude of the different discontinuities are listed in Table 4. In what follows, the amplitude of seismic discontinuities are given in percents. The percentages are computed with respect to the nominal values of PREM at 670 km depth. Uncertainties on the amplitudes of anomalies are obtained in the following way: two additional sets of elastic data are derived from Table 2, by varying the different elastic parameters within their experimental uncertainties. The first data set is built in order to increase the seismic

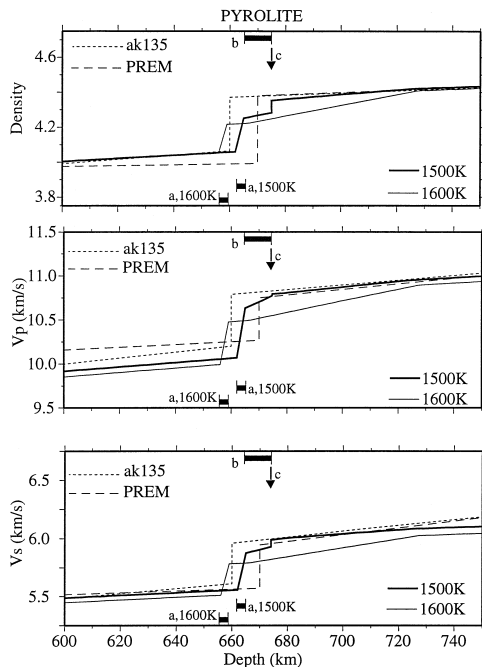


Fig. 7. Computed profiles between 600 and 750 km depth, for a pyrolite composition. Globally averaged seismic profiles are PREM (Dziewonski and Anderson, 1981; long-dashed lines) and ak135 (short-dashed lines). Bold (thin) lines correspond to profiles computed along the 1500 K (1600 K) adiabat. The different reactions at different temperatures are located by black bands or arrows near the horizontal axis, and labelled: (a)  $\gamma$ -spinel  $\rightarrow$  Mg-perovskite + Mg-wüstite, (b) garnet  $\rightarrow$  garnet + ilmenite, (c) garnet + ilmenite  $\rightarrow$  garnet + perovskite.

velocities of Mg-perovskite and Mg-wüstite, and decrease the seismic velocities of ilmenite; the second data set increases the seismic velocities of ilmenite and decreases the ones of Mg-perovskite and Mg-wüstite. Using these two extreme data sets, we estimate the maximum amplitude variations of each discontinuity due to experimental uncertainties. We first pay attention to the results obtained using the updated experimental values of Table 2. Then, the very large uncertainties involved by both extreme data sets are discussed.

### 6.1. Pyrolite composition

The transition from  $\gamma$ -spinel to Mg-perovskite + Mg-wüstite (located along the bottom horizontal axis of each plot and labelled 'a') induces a sharp increase of density between 662 and 665 km depth,

equal to 4.8% and 4.1% along the 1500 K and 1600 K, respectively. These jumps are about twice smaller than the density jumps observed in radial seismic models (7.7 and 9.7% in ak135 and PREM, respectively). Along the 1500 K adiabat, the two reactions involving ilmenite are located at the top of each plot and labelled 'b' for garnet  $\rightarrow$  garnet + ilmenite and 'c' for garnet + ilmenite  $\rightarrow$  garnet + perovskite. They lead to density jumps of 0.8% and 1.8% and occur at depths of 665–675 and 675 km, respectively. The total amplitude of the three discontinuities along the 1500 K adiabat is 7.4%, in good agreement with radial seismic models. Hence the reactions occurring in the non-olivine part of the mineralogy are required, together with the breakdown of  $\gamma$ -spinel, in order to explain the observed density jump at 660 km depth with a pyrolitic composition.

Results are slightly different for seismic velocities. P- and S-wave velocity jumps due to the breakdown of  $\gamma$ -spinel are 5.5% and 5.7% along the 1500 K adiabat, and 4.7% and 4.9% along the 1600 K adiabat, respectively. These predicted jumps are in

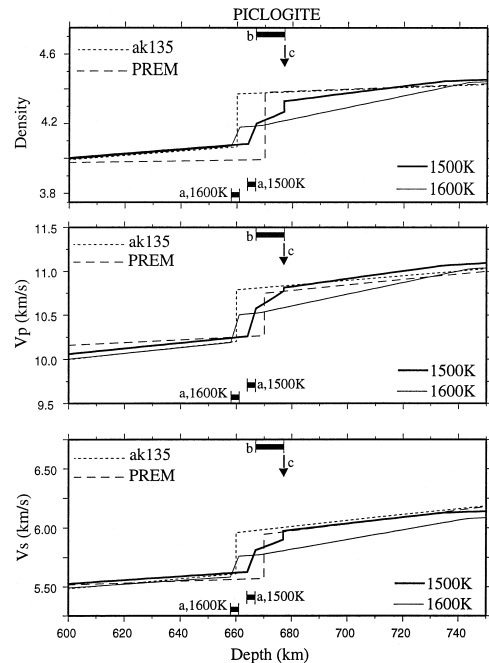


Fig. 8. Same as Fig. 7, for a piclogite composition. (a)  $\gamma$ -spinel  $\rightarrow$  Mg-perovskite + Mg-wüstite, (b) garnet  $\rightarrow$  garnet + ilmenite, (c) garnet + ilmenite  $\rightarrow$  garnet + perovskite.

Table 4

Amplitude of the different velocity jumps (in %), for each reaction

		1000 K		1500 K		1600 K	
		Pyrolite	Piclogite	Pyrolite	Piclogite	Pyrolite	Piclogite
a	<i>z</i>	690–693	692–694	662–665	664–667	656–659	658–661
	$\rho$	$5.0 \pm 0.2$	$3.3 \pm 0.1$	$4.8 \pm 0.2$	$2.9 \pm 0.2$	$4.1 \pm 0.2$	$2.8 \pm 0.2$
	$V_p$	$4.3 \pm 2.4$	$2.8 \pm 1.4$	$5.5 \pm 3.0$	$3.1 \pm 2.0$	$4.7 \pm 3.0$	$3.1 \pm 2.2$
	$V_s$	$5.6 \pm 3.7$	$3.6 \pm 2.2$	$5.7 \pm 4.0$	$3.3 \pm 3.0$	$4.9 \pm 5.0$	$3.2 \pm 3.5$
b	<i>z</i>			665–675	667–677		
	$\rho$			$0.8 \pm 0.1$	$1.7 \pm 0.2$		
	$V_p$			$1.4 \pm 0.6$	$1.9 \pm 1.0$		
	$V_s$			$1.1 \pm 0.5$	$0.5 \pm 1.0$		
c	<i>z</i>			675	677		
	$\rho$			$1.8 \pm 0.2$	$1.6 \pm 0.2$		
	$V_p$			$0.2 \pm 3.0$	$0.4 \pm 3.0$		
	$V_s$			$1.1 \pm 4.0$	$1.4 \pm 3.8$		
d	<i>z</i>	608–664	638–676				
	$\rho$	$2.6 \pm 0.2$	$3.0 \pm 0.3$				
	$V_p$	$3.1 \pm 1.1$	$3.2 \pm 1.3$				
	$V_s$	$2.7 \pm 1.1$	$3.1 \pm 4.2$				
e	<i>z</i>	709–731	711–733				
	$\rho$	$2.4 \pm 0.2$	$3.2 \pm 0.4$				
	$V_p$	$1.4 \pm 2.9$	$1.8 \pm 3.5$				
	$V_s$	$3.0 \pm 3.5$	$3.9 \pm 4.5$				
Cumul.	$\rho$	$10.0 \pm 0.2$	$9.5 \pm 0.2$	$7.4 \pm 0.2$	$6.2 \pm 0.4$		
	$V_p$	$8.7 \pm 4.0$	$7.8 \pm 3.8$	$7.1 \pm 5.0$	$5.4 \pm 4.0$		
	$V_s$	$11.3 \pm 6.0$	$10.6 \pm 6.0$	$7.9 \pm 8.0$	$6.3 \pm 6.0$		
Refer.	$\rho$				$8.7 \pm 1.0^f$		
	$V_p$	$4.0^g$			$5.2 \pm 2.0^f$		
	$V_s$	$7.4^h$			$6.5 \pm 2.0^f$		

The reactions are: a:  $\gamma$ -spinel  $\rightarrow$  perovskite + Mg-wüstite; b: garnet  $\rightarrow$  garnet + ilmenite; c: garnet + ilmenite  $\rightarrow$  garnet + perovskite; d: garnet  $\rightarrow$  ilmenite; e: ilmenite  $\rightarrow$  perovskite; Cumul.: cumulative effect of the reactions.

For each discontinuity, the depth interval (*z*) is given in km; each percentage is computed with respect to the corresponding value of PREM (Dziewonski and Anderson, 1981) at 670 km depth. See text for the meaning of uncertainties. Note that density jumps are better constrained than seismic velocities. This is mainly due to the large experimental uncertainties on the elastic moduli of perovskites. Observed discontinuities in reference are: f: averages between discontinuities of ak135 (Kennett et al., 1995) and PREM; errors are estimated after Kennett (1991); g: S25 (Lefevre and Helmberger, 1989); h: SNA (Grand and Helmberger, 1984).

good agreement with observed P- and S-wave discontinuities (5.2% and 6.5%, respectively), although the predicted S-wave jump is 10 to 25% smaller than the observed one. Along the 1500 K adiabat, reactions involving the presence of ilmenite add substantial amplitudes (see Table 4 for details), leading to total P- and S-wave jumps of 7.1% and 7.9%, respectively. These values are 20–35% higher than the seismically observed amplitudes. Therefore, on the basis of seismic velocities and with a starting composition of pyrolite, the temperature profile that does not cross the stability field of ilmenite (1600 K) gives a slightly better explanation to seismically observed discontinuities. However this conclusion is

dependent on the large experimental uncertainties (cf. below).

Besides the amplitude of the discontinuities around 660 km depth, the layer at the top of the mantle (down to a depth of 750 km, say) must be considered. Radial seismic models report high seismic gradients in this layer. Such high gradients are also confirmed by recent studies on PP and SS precursors (Shearer, 1996; Schimmel, 1997). Table 5 gives the density, P- and S-wave gradients computed along the 1500 K and 1600 K adiabats, together with observed gradients in PREM and ak135. Note that these reference models do not show any strong density gradient at the top of the lower mantle, but rather a constant

Table 5

Density and seismic velocity gradients at the top of the lower mantle, under the assumption of a whole mantle convection

Gradient	1500 K		1600 K		Observed
	Pyrolite	Piclogite	Pyrolite	Piclogite	
$d\rho/dz$ ( $10^{-4}$ kg m $^{-4}$ )	$13.1 \pm 0.4$	$20.1 \pm 0.5$	$28.3 \pm 0.7$	$31.4 \pm 0.5$	$6.1 \pm 0.1$
$dV_p/dz$ ( $10^{-3}$ s $^{-1}$ )	$3.2 \pm 1.2$	$4.4 \pm 2.2$	$6.1 \pm 4.0$	$6.2 \pm 3.9$	$2.9 \pm 0.3$
$dV_s/dz$ ( $10^{-3}$ s $^{-1}$ )	$1.7 \pm 1.0$	$2.7 \pm 2.0$	$3.5 \pm 3.0$	$3.9 \pm 3.1$	$2.7 \pm 0.6$

Observed gradients are averages between gradients of ak135 (Kennett et al., 1995) and PREM (Dziewonski and Anderson, 1981); errors are estimated after Kennett (1991).

density gradient down to the core mantle boundary. Theoretical gradients are calculated between the deepest discontinuity (garnet + ilmenite  $\rightarrow$  garnet + perovskite) and the complete vanishing of garnet in the lower mantle (between 720 and 740 km depth for the different cases). Along the 1500 K adiabat (presence of ilmenite), the density gradient is twice higher than the observed ones ( $13.1 \times 10^{-4}$  kg m $^{-4}$  vs.  $6.1 \times 10^{-4}$  kg m $^{-4}$ ), and the seismic gradients are in relatively good agreement with the observations:  $3.2 \times 10^{-3}$  s $^{-1}$  vs.  $2.9 \times 10^{-3}$  s $^{-1}$  for P-wave;  $1.7 \times 10^{-3}$  s $^{-1}$  vs.  $2.7 \times 10^{-3}$  s $^{-1}$  for S-wave. Along the 1600 K profile (no ilmenite involved), the computed gradients are doubled ( $28.3 \times 10^{-4}$  kg m $^{-4}$ , 6.1 and  $3.5 \times 10^{-3}$  s $^{-1}$  for density P- and S-wave, respectively), leading to a worse comparison with observed gradients. Note that here the computed density gradient is about five times greater than the observed one. We believe this discrepancy to be very conclusive: if such a high density gradient was real, it should be observed in seismic reference models. These differences between the 1500 and 1600 K adiabats are due to the presence of ilmenite along the coldest one, and to its ability to consume the most part of the garnet: along the 1500 K, only 7% of garnet are still present after the disappearing of ilmenite, whereas the top of the lower mantle contains 28% of garnet along the 1600 K adiabat. Therefore, with a pyrolite composition, the presence of ilmenite is required around 660 km depth to give a good explanation of the seismic gradients at the top of the lower mantle.

The joint analysis of instantaneous jumps around 660 km depth and gradients at the top of the lower mantle clearly points out two groups of profiles: the junction from the mantle transition zone to the deep lower mantle can be made either by (1) strong

instantaneous discontinuities followed by relatively small gradients (case of stable ilmenite, illustrated by the 1500 K adiabat), or (2) relatively small discontinuities followed by high gradients (no ilmenite, case illustrated by the 1600 K adiabat). The former case gives the best explanation to actual reference seismic models.

## 6.2. Piclogite composition

Computed profiles obtained with a piclogite starting composition are shown in Fig. 8, and amplitudes of the seismic jumps are listed in Table 4. The density jumps due to the breakdown of  $\gamma$ -spinel obtained along both adiabats have values of the order of 2.8%, three times smaller than the observed ones; the P- and S-wave velocity jumps due to this reaction are around 3.2%, about twice smaller than the seismically derived discontinuities. Therefore, with a piclogite composition, the breakdown of  $\gamma$ -spinel alone drastically fails to explain the amplitude of the 660 km depth discontinuity. On the other hand, the consideration of the two reactions involving ilmenite along the 1500 K adiabat gives total seismic jumps in agreement with observations (5.4% vs. 5.2% for P-waves, 6.3% vs. 6.5% for S-waves). Still, the cumulative density jump is 6.2%, 30% smaller than the seismically derived discontinuity. Concerning the computed gradients at the top of the lower mantle (Table 5), the conclusion reached for the pyrolitic models is also valid here: gradients computed along the 1600 K adiabat (no ilmenite,  $31.4 \times 10^{-4}$  kg m $^{-4}$ , 6.2 and  $3.9 \times 10^{-3}$  s $^{-1}$  for density, P- and S-wave velocities, respectively) are 30% higher than the ones computed along the 1500 K adiabat (presence of ilmenite,  $20.1 \times 10^{-4}$  kg m $^{-4}$ , 4.4 and  $2.7 \times 10^{-3}$  s $^{-1}$ ). Therefore, reactions involving il-

menite are also required to fit the lower mantle seismic gradients at best. Note that the difference between gradients computed along the two adiabats are much smaller here than in the pyrolitic case, for a reason that has already been mentioned: these high gradients are due to the presence of garnet, and the role of ilmenite as a consumer of garnet along the 1500 K is attenuated in piclogite, because of its higher  $\text{Al}_2\text{O}_3$  content.

### 6.3. Extreme data set

The experimental uncertainties on elastic parameters induce large uncertainties on the amplitude of the seismic jumps. This is particularly true for lower mantle minerals; for instance, the value of  $\dot{G}$  for Mg-perovskite is derived from elasticity systematics, and is known with an accuracy lower than 35% (Duffy and Anderson, 1989). Consequently, the errors bars on the computed amplitudes are very large, reaching 100% of the proposed value for some numbers (Tables 4 and 5). Of course the extreme jumps

proposed here are unrealistic, but they ensure that the actual amplitudes of the seismic jumps lie within the computed domains of variation, and they document how independent from experimental uncertainties our conclusions are.

Fig. 9 gives a synthetic summary of the results presented so far. Each of the four panels represents computed amplitudes of discontinuities (squares and triangles) and computed seismic gradients (circles), as a function of the corresponding observed values. The diagonal line represents the perfect fit between predictions and observations. Note that amplitudes (in %) and seismic gradients (in  $10^{-3} \text{ s}^{-1}$ ) are plotted on the same scale. The top left panel corresponds to the 1500 K profiles, and therefore cumulative amplitudes of the three reactions are plotted; the top right panel corresponds to the 1600 K profiles, and amplitudes due to the breakdown of  $\gamma$ -spinel (the only sharp reaction to occur) are plotted. Both panels show the pyrolite composition results. A visual comparison clearly shows that the 1500 K profile (presence of ilmenite) gives much better explana-

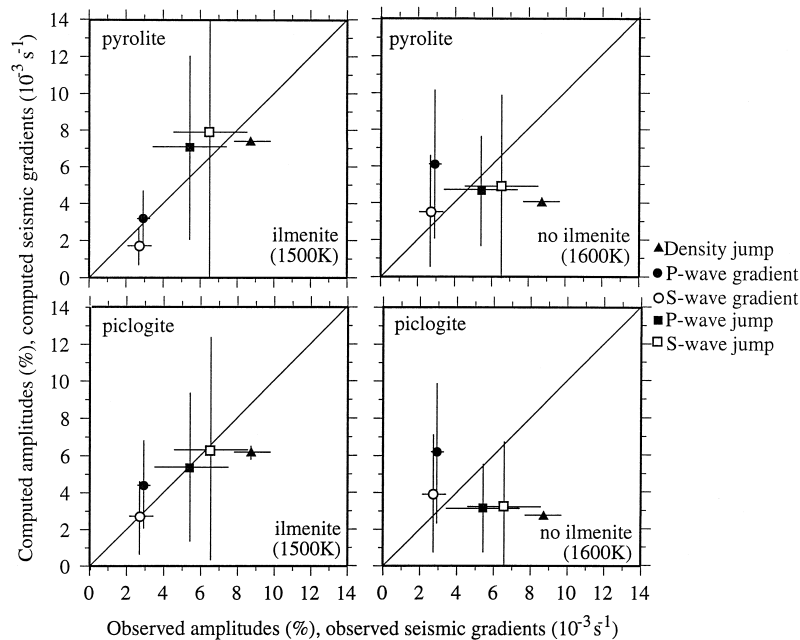


Fig. 9. Computed parameters as a function of corresponding observed parameters. Circles: seismic gradients (in  $10^{-3} \text{ s}^{-1}$ ); squares: amplitude of seismic jumps (in %); black and white symbols hold for P- and S-wave velocities, respectively; triangles: amplitude of density jumps (in %). Top panels are for a pyrolite composition, bottom panels are for a piclogite composition. Left panels: results along the 1500 K adiabat (presence of ilmenite); right panels: results along the 1600 K adiabat (no stable ilmenite). Vertical error bars are not plotted if they are smaller than symbol sizes.

tions of seismic gradients (circles) and density jumps (triangles) than the 1600 K profile (no ilmenite) does. A mixed conclusion is found for seismic velocity jumps (square): the P-wave observed jumps are better retrieved along the 1600 K profiles (without ilmenite), and the S-wave jumps are equally fitted by either of the 1500 or 1600 K profiles. Unfortunately, the errors bars are too large to remove any of the models, and it is not possible to strengthen our conclusions in case of a pyrolite starting composition.

Conversely, results are unambiguous with a piclogite starting composition (bottom panels). Whatever the considered parameter (density of seismic gradients, density or seismic discontinuities), observations are better matched with the presence of ilmenite (1500 K profiles) than without ilmenite (1600 K profiles). This conclusion still holds when experimental uncertainties are taken into account (vertical error bars): along the 1600 K profiles (right panel), only the S-wave velocity gradients can be fitted with reasonable variations of the elastic parameters within their uncertainties. Other parameters would require extreme data sets to fit observations. We therefore conclude that, if the mantle has a piclogite composition, the non-olivine part of the mineralogy plays a crucial role, and the presence of ilmenite around 660 km depth is required to explain the horizontally averaged seismic models.

## 7. The nature of the 660 km depth discontinuity in subduction zones

Fig. 10 shows the computed profiles along the 1000 K adiabat, for pyrolite and piclogite starting compositions. The amplitudes of the different discontinuities are listed in Table 4. Many common features are obtained whatever the composition. The three reactions occurring between 600 and 750 km depth are now separated. The first reaction (labelled 'd' in Fig. 10 and Table 4), garnet  $\rightarrow$  ilmenite, is very broad, and appears within the depth ranges 608–664 km for pyrolite, and 638–676 km for piclogite. This difference of location at depth is due to the alumina enrichment of piclogite. The amplitudes of density, P- and S-wave discontinuities are respectively  $2.6 \pm 0.2\%$ ,  $3.1 \pm 1.1\%$  and  $2.7 \pm 1.1\%$  for

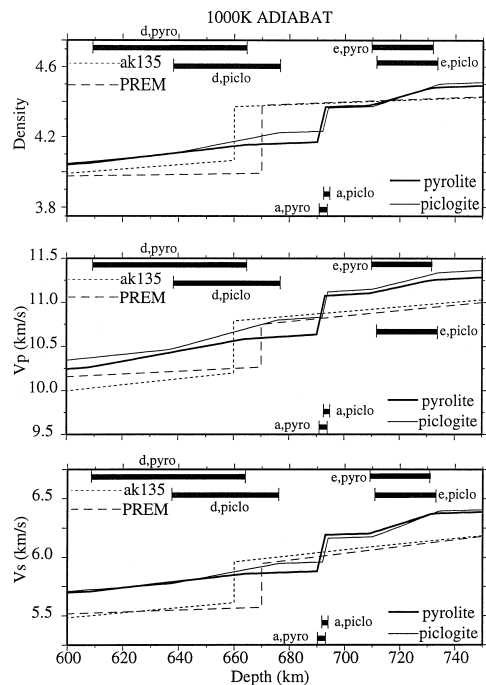


Fig. 10. Computed profiles along the 1000 K adiabat. Bold (thin) lines are for a pyrolite (piclogite) composition. The different reactions are labelled together with the corresponding composition (pyro for pyrolite and piclo for piclogite). (a)  $\gamma$ -spinel  $\rightarrow$  Mg-perovskite + Mg-wüstite, (d) garnet  $\rightarrow$  ilmenite, (e) ilmenite  $\rightarrow$  perovskite.

pyrolite, and  $3.0 \pm 0.3\%$ ,  $3.2 \pm 1.3\%$  and  $3.1 \pm 1.4\%$  for piclogite. Then, the breakdown of  $\gamma$ -spinel takes place at depths of 690–693 km for pyrolite, 692–694 km for piclogite, respectively. Amplitudes of discontinuities are  $5.0 \pm 0.2\%$ ,  $4.3 \pm 2.4\%$  and  $5.6 \pm 3.7\%$  for pyrolite, and  $3.3 \pm 0.1\%$ ,  $2.8 \pm 1.4\%$  and  $3.6 \pm 2.2\%$  for piclogite, respectively for density, P- and S-wave velocities. As one could expect, higher amplitudes are found with pyrolite (higher bulk olivine content). Finally, the reaction ilmenite  $\rightarrow$  perovskite (labelled 'e') occurs at 709–731 (711–733) km depth for pyrolite (piclogite). Amplitudes are  $2.4 \pm 0.2\%$ ,  $1.4 \pm 2.9\%$  and  $3.0 \pm 3.5\%$  for pyrolite, and  $3.2 \pm 0.4\%$ ,  $1.8 \pm 3.5\%$  and  $3.9 \pm 4.5\%$  for piclogite. Once more, the uncertainties on the actual amplitudes of seismic jumps are very large, but we can conclude that a multi-step transition from the upper to the lower mantle, with three separate discontinuities, must be found in cold regions of the mantle. The discontinuity due to the breakdown of  $\gamma$ -spinel is very sharp



(about 2 km thickness), whereas the two discontinuities related to ilmenite span much broader depth intervals (22 to 56 km thicknesses). Note that the thickness of the garnet  $\rightarrow$  ilmenite discontinuity is a function of the  $\text{Al}_2\text{O}_3$  content of the mantle: it is thinner in piclogite (38 km thick) than in pyrolite (56 km thick). Comparing qualitatively the amplitudes of the different discontinuities, the starting composition has an important effect: with a pyrolite composition, discontinuities due to the breakdown of  $\gamma$ -spinel ('a') and ilmenite  $\rightarrow$  perovskite ('e') have similar, relatively high amplitudes, whereas garnet  $\rightarrow$  ilmenite ('d') induces a discontinuity with a two to three times smaller amplitude. With a piclogite composition,  $\gamma$ -spinel  $\rightarrow$  Mg-perovskite + Mg-wüstite ('a') and garnet  $\rightarrow$  ilmenite ('d') have similar, relatively small amplitudes whereas ilmenite  $\rightarrow$  perovskite ('e') gives amplitudes that are three times higher. Again, the bulk olivine and  $\text{Al}_2\text{O}_3$  contents of the mantle have important signatures on the discontinuity pattern.

The cumulative density, P- and S-wave velocity jumps due to the three reactions are respectively  $10.0 \pm 0.2\%$ ,  $8.7 \pm 4.0\%$  and  $11.3 \pm 6.0\%$  for pyrolite, and  $9.5 \pm 0.2\%$ ,  $7.8 \pm 3.8\%$  and  $10.6 \pm 6.0\%$  for piclogite. For comparison, seismically observed discontinuities in cold regions are listed in Table 4:  $\delta V_p/V_p = 4.0\%$  (model of the Canadian shield, S25, Lefevre and Helmberger, 1989);  $\delta V_s/V_s = 7.4\%$  (model of the north American continent, SNA, Grand and Helmberger, 1984). It is important to keep in mind that these models have been constructed with one single discontinuity imposed a priori at the upper–lower mantle transition. The cumulative amplitudes of the three discontinuities are 30 to 60% higher than the observed jumps. Some explanations of these discrepancies between predictions and observations can be found: the two reactions involving ilmenite are very broad, and they might be included into the seismic gradients of upper mantle seismic models (note also that seismic gradients are badly constrained around 600–700 km depth in radial seismic models, Kennett, 1991); from an other point of view, if the actual amplitudes are close to the lowest extreme values defined by experimental uncertainties (see Table 4 and above numbers), the corresponding discontinuities might be seismically invisible.

## 8. Discussion

The appearance of ilmenite at a depth of 660 km along the horizontally averaged temperature profile is closely dependent on the chosen adiabatic profile. To our knowledge, it has not been reported before, because previous studies always considered adiabats with higher foot temperatures to be representative of the upper mantle: 1673 K (Bass and Anderson, 1984; Duffy and Anderson, 1989), 1700 K (Ita and Stixrude, 1992). Stixrude et al. (1992) reported that a 1500 K adiabat gives the best fit to upper mantle seismic data, but claimed that this temperature was 'unreasonably too cold'. We would like to remind here four independent results of different geophysical fields, which all show that a 1500 K adiabat is likely to be representative of the upper mantle: (1) precise thermodynamic calculations applied to seismic data give a temperature of 1588 K at a depth of 270 km (Brown and Shankland, 1981); (2) petrological studies of xenoliths (geothermometry and geobarometry) lead to a temperature of  $1600 \pm 200$  K at a depth of 200 km (Jeanloz and Morris, 1986); (3) the phase transition from  $\alpha$ -olivine to  $\beta$ -spinel, which appears at a depth of 410 km, occurs at a temperature of  $1700 \pm 100$  K (Katsura and Ito, 1989); (4) convection experiments with strongly variable viscosity suggest that the value of the temperature at the base of the conductive lithosphere (80 km depth) is close to 1520 K (Davaille and Jaupart, 1994). Using a temperature gradient of  $0.4 \text{ K km}^{-1}$  for the upper most mantle (Vacher et al., 1996), all these independent studies converge to a surface temperature of 1500 K, and hence ilmenite is likely to occur along the horizontally averaged temperature profile of the mantle around 670 km depth.

### 8.1. Stratification of the mantle

The results shown in this study are all based on the assumption of a single layer mantle convection. Hence, no thermal boundary layer has been considered at the top of the lower mantle, and the upper and lower mantles have the same global composition (pyrolite or piclogite). However, it is also reasonable to consider a layered convection, as suggested by geochemical arguments (e.g., Allègre and Turcotte,

1986). Then it is likely that the mean temperature of the lower mantle is larger than the mean temperature of the upper mantle, due to the presence of a thermal boundary layer at the top of the lower mantle; it is also likely that the upper and lower mantle have different compositions, since they are independently convecting. This case is studied by putting a 250 K thermal boundary layer just below the depth of the  $\gamma$ -spinel breakdown. Numerical experiments of fluids heated from below (core) and within suggest that the convective planform in the lower mantle would be dominated by cold downwellings (e.g., Tackley, 1993; Sotin and Labrosse, 1997). Furthermore, if a thermal coupling exists between both cells as proposed by Anderson (1981), the cold adiabat in the upper mantle can be continued in the lower mantle. The cold slabs lay at the 670 km discontinuity and impose the temperature of the cold downwellings in the lower mantle. It might hence be impossible to distinguish between one and two cells in cold regions of the mantle. Following the mantle evolution model of Anderson (1983), we consider that the lower mantle is entirely composed of MgO, SiO<sub>2</sub> and FeO, the other oxides being incorporated in the primitive ‘magma ocean’. This induces a lower mantle composition with 84% of perovskite and 16% Mg-wüstite (Zhao and Anderson, 1994). We use an iron partitioning coefficient equal to  $K_{\text{Mg-Fe}}^{\text{Pv-Mw}} = 0.4$  for this Al-free lower mantle (Katsura and Ito, 1996; Martinez et al., 1997). Fig. 11 shows the profiles computed with this model. Along the adiabat simulating the horizontally averaged temperature of the mantle, the boundary between the pyrolitic upper mantle and the assemblage of perovskite and Mg-wüstite (marked by arrows) gives a good fit to observed discontinuities: density, P- and S-wave velocities increase by  $7.1 \pm 0.2\%$ ,  $6.6 \pm 7.3\%$  and  $5.8 \pm 10.0\%$  with respect to PREM values, respectively. Note the very large error domains, due to the very large uncertainties on temperature derivatives of elastic moduli for Mg-perovskite (Table 2). Again, the extreme jumps reported here would be followed by extreme and unrealistic velocity profiles. However, the agreement between the above amplitudes and the observed ones here is essentially as good as the agreement obtained in the previous sections for the case of a whole mantle convection. This is due to the counteracting effects of the thermal boundary

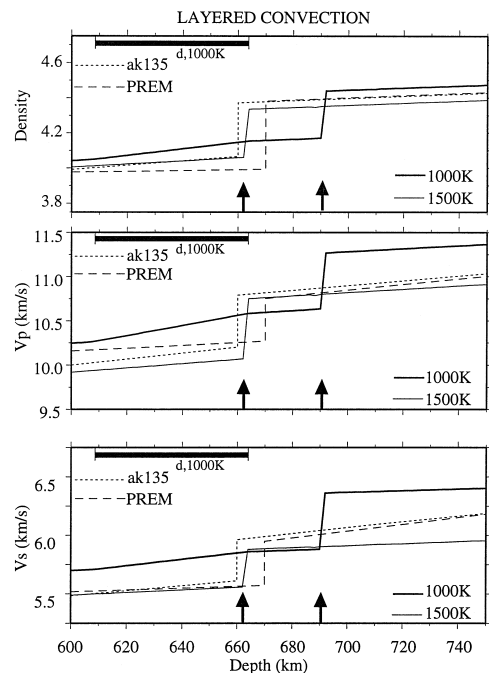


Fig. 11. Computed profiles for a layered mantle convection model (see text for description). Bold (thin) lines are for the 1000 K (1500 K) profiles. The arrows indicate the depth of the chemical boundary. Reaction ‘d’ (garnet  $\rightarrow$  ilmenite) still occurs along the 1000 K temperature profile.

and chemical differentiation on seismic parameters. We therefore end with the same conclusion as Stixrude et al. (1992) or Zhao and Anderson (1994): the interpretation of seismic data using mineral physics fails to discriminate between a whole mantle and a layered convection.

Along the cold temperature profile, two discontinuities appear: first, garnet transforms into ilmenite in the pyrolitic upper mantle in the depth range 608–664 km (reaction ‘d’, located at the top of each plot), yielding density, P- and S-wave jumps equal to  $2.6 \pm 0.2\%$ ,  $3.1 \pm 1.1\%$  and  $2.7 \pm 1.0\%$ , respectively. Then, the boundary between the pyrolitic upper mantle and the lower mantle occurs at 690–692 km depth, with density, P- and S-wave increases of the order of  $6.7 \pm 0.4\%$ ,  $6.1 \pm 6.0\%$  and  $8.6 \pm 8.0\%$ , respectively. We want to point out this double discontinuity in the cold profile: whatever the chosen scenario for mantle convection, ilmenite appears in cold regions of the upper mantle, inducing a significant seismic discontinuity. We therefore believe that

several discontinuities are more likely to exist in subduction zones than one single depth discontinuity.

## 8.2. Seismic observations of mantle discontinuities

Many seismic observations of the mantle discontinuities have been successfully compared to predicted phase transformations in the olivine phase diagram. First, the thickness of the 410 km depth discontinuity has been found to vary between 2 and 35 km (Vidale et al., 1995), in a good agreement with the pressure range of coexistence of  $\alpha$ -olivine and  $\beta$ -spinel in the mantle transition zone (Katsura and Ito, 1989; Fei et al., 1990). Conversely, the thickness of the 670 km depth discontinuity has been found to be much smaller, at most 5 km thick (Paulssen, 1988; Yamazaki and Hirahara, 1994), in a good agreement with the sharp transition from  $\gamma$ -spinel to Mg-perovskite + Mg-wüstite (Ito and Takahashi, 1989). Furthermore, studies of the topography variations of these discontinuities have shown a negative correlation between the respective deflections of the '410' and the '660' (Revenaugh and Jordan, 1991; Vidale and Benz, 1992; Shearer, 1993). This is also in agreement with the opposite signs of the Clapeyron slopes of the respective transitions in the olivine system. Some features of the proposed explanation of the 660 km discontinuity in this paper are consistent with these observations.

The occurrence of ilmenite along the cold temperature profile leads to three separate discontinuities, at respective depths of 608–664 km (exothermic appearance of ilmenite), 690–693 km (endothermic breakdown of  $\gamma$ -spinel), and 709–731 km (endothermic vanishing of ilmenite, depths are given for a pyrolitic composition). Recent seismic observations support this complex pattern for cold regions of the mantle. First, studies of multiple ScS reverberations found some complexity in the vicinity of the 660 km depth discontinuity, with short scale lateral variations of the reflection coefficient of this discontinuity (Revenaugh and Jordan, 1991; Revenaugh and Sipkin, 1994). These latter authors attributed these variations to the stagnation of the cold slab atop the 660 km discontinuity (Fukao et al., 1992). They also found a 'lower mantle' discontinuity at 710 km depth, that we might attribute to the vanishing of ilmenite. A strong support to our interpretation comes from the results of Niu and Kawakatsu (1996). Computing a

'discontinuity response function' of broadband seismic data under three stations in Japan and Northeast China, Niu and Kawakatsu (1996) clearly found no depression of the 660 km discontinuity, but rather a complex structure with three separate discontinuities between 660 and 780 km depth. This complex structure is restricted to the tip of the subducting slab, and only one discontinuity appears beneath the two stations away from the slab. Furthermore, the three discontinuities revealed within the tip of the slab have nearly the same impedance contrast, in some agreement with our predictions. The signals associated with these three transitions vanish in the 2–5 s period range commonly used for P–S conversion phases; this frequency dependence explains why the 660 km discontinuity has been previously interpreted as a single discontinuity. Therefore the explanation of the '660' discontinuity involving the presence of ilmenite can find some support in recent seismic observations. Further observations of this discontinuity, including broadband waveforms, are needed to definitively confirm this present explanation.

Some recent seismic studies of precursors to PP (Estabrook and Kind, 1996), and P–S conversions (e.g., Bock and Kind, 1991; Niu and Kawakatsu, 1996) found that deviations from classical globally averaged models were needed to fit their data. Estabrook and Kind (1996) proposed a 2% P-wave velocity jump for the 660 km depth discontinuity, together with the density and S-wave velocity jumps given by PREM or ak135. They interpreted these features by a  $\Delta\lambda = 0$  ( $\lambda$  being the first Lamé parameter) across the upper–lower mantle boundary. In a previous version of the present paper, based on older elastic numbers (coming mainly from elasticity systematics), we found very small P-wave velocity jumps, in close agreement with the results and interpretations of Estabrook and Kind (1996). It is not true anymore with the new elastic data compilation given here: with a pyrolite starting composition, we find now an increase of  $\lambda$  equal to  $15 \pm 2\%$  at 660 km depth, very close to the increase reported in PREM (17%). However, a much smaller jump in Lamé parameter cannot be ruled out from our modelling, given the large uncertainties on our results. Note that the  $\lambda$  parameter is much better constrained in our calculations than seismic velocities are, because most of experimental uncertainties concern the

shear moduli. This last comparison between seismic studies and mineralogical models points out the need of further investigations both in seismological modelling and experimental mineralogy, before getting a consensus on the physical properties of the upper–lower mantle transition.

## 9. Conclusion

The large number of experimental works in the past few years enabled us to review the elastic data and phase relations relevant to mantle minerals. Using this new elastic data compilation and the methods described by Ita and Stixrude (1992) and Vacher et al. (1996), theoretical profiles of density and seismic velocities have been computed. A single layer convection and a chemically homogeneous mantle have been assumed for this purpose. Three different temperature profiles have been used to study cold regions (subduction zones) and two different cases for the horizontally averaged mantle. Two starting compositions, pyrolite and piclogite, were considered. The non-olivine part of the mineralogy is shown to display strong density and seismic jumps, and to play a crucial role for the explanation of density and seismic profiles. Two possibilities show up at the upper–lower mantle transition. (1) Ilmenite appears at the expense of garnet and then transforms into perovskite plus a small amount of garnet (case illustrated by the 1500 K adiabat). In such a case, strong seismic discontinuities are found around 660 km depth, due to the cumulative effects of the breakdown of  $\gamma$ -spinel and the reactions involving ilmenite. Then, relatively small seismic gradients are found at the top of the lower mantle. (2) Ilmenite is not stable around 660 km depth, and the entire garnet content of the upper mantle gradually transforms into perovskite at the top of the lower mantle (case illustrated by the 1600 K adiabat). This induces smaller discontinuities (the breakdown of  $\gamma$ -spinel is the only reaction to occur) and very high gradients at the top of the lower mantle. Although the possible variations in these synthetic results are very high due to experimental uncertainties, the comparison with globally averaged seismic models favours the former case with stability of ilmenite.

Along the cold temperature profile, three reactions occur at three separate depths, leading to three

separate discontinuities. Depth location, thickness and amplitude of these discontinuities depend on the bulk mantle composition. Such a complex pattern has been observed in recent seismic studies in subduction zones. A case of stratified mantle convection has also been studied, including a thermal boundary layer and different compositions between the upper and the lower mantles. This case also provides a relatively good fit to observed discontinuities, and hence it is not possible to definitively distinguish between a single layer and a stratified mantle convection using this method. Ilmenite still appears in the upper mantle in that scenario, leading to an additional phase transition preceding the chemical boundary along the cold temperature profile. We therefore propose that the multiple step transition from the upper to the lower mantle in subduction zone, with at least two discontinuities, is a robust feature.

Further experimental work is required to better define the stability field of ilmenite around 22–24 GPa. This would bring new constraints on the temperature profile of the Earth's mantle, since seismic data require the presence of ilmenite at 660 km depth.

## Acknowledgements

We thank C.R. Bina, F. Guyot, P. Lognonné, B. Reynard and J. Trampert for helpful discussions, G. Cornen and C. Monnier for their help in the computations needed for Table 1, and C. H. Estabrook and F. Niu for sending their papers prior to publication. Two anonymous reviewers provided thorough comments and critics which helped us to revise a first version of the manuscript. This work was started during PV's PhD thesis, funded by French Ministry of Research, and continued at Utrecht University in the framework of Pionier Project PGS 76-144, funded by NWO. It was partially funded by INSU/CNRS under contracts 94TOM02 and 97IT55.

## References

- Abramson, E.H., Brown, J.M., Slutsky, L.J., Zaug, J., 1997. The elastic constants of San Carlos olivine to 17 GPa. *J. Geophys. Res.* 102, 12253–12263.
- Akaogi, M., Ito, E., Navrotsky, A., 1989. Olivine-modified

- spinel–spinel transitions in the system  $\text{Mg}_2\text{SiO}_4$ – $\text{Fe}_2\text{SiO}_4$ : calorimetric measurements, thermochemical calculation, and geophysical application. *J. Geophys. Res.* 94, 15671–15685.
- Akaogi, M., Ito, E., 1993. Refinement of enthalpy measurement of  $\text{MgSiO}_3$  perovskite and negative pressure–temperature slopes for perovskite-forming reactions. *Geophys. Res. Lett.* 20, 1839–1842.
- Allègre, C.J., Turcotte, D.L., 1986. Implications of a two-component marble cake mantle. *Nature* 323, 123–127.
- Anderson, D.L., 1981. A global chemical model for the evolution of the mantle. In: O'Connell, R.J., Fyfe, W.S. (Eds.), *Evolution of the Earth*. Am. Geophys. Union, *Geodynamics series* 5, 6–18.
- Anderson, D.L., 1983. Chemical composition of the mantle. *J. Geophys. Res.* 88, B41–B52.
- Anderson, D.L., Bass, J.D., 1986. Transition region of the Earth's upper mantle. *Nature* 320, 321–328.
- Anderson, O.L., 1997. Finding the isentropic density of perovskite: implications for iron concentration in the lower mantle. *Geophys. Res. Lett.* 24, 213–216.
- Anderson, O.L., Isaak, D.L., Oda, H., 1991. Thermoelastic parameters for six minerals at high temperature. *J. Geophys. Res.* 96, 18037–18046.
- Angel, R.J., Hugh-Jones, D.A., 1994. Equations of state and thermodynamic properties of enstatite pyroxenes. *J. Geophys. Res.* 99, 19777–19783.
- Ashida, T., Kume, S., Ito, E., Navrotsky, A., 1988.  $\text{MgSiO}_3$  ilmenite: heat capacity, thermal expansivity and enthalpy of transformation. *Phys. Chem. Miner.* 16, 239–245.
- Bass, J.D., Anderson, D.L., 1984. Composition of the upper mantle: geophysical tests of two petrological models. *Geophys. Res. Lett.* 11, 237–240.
- Bina, C.R., 1995. Confidence limits for silicate perovskite equations of state. *Phys. Chem. Miner.* 22, 375–382.
- Bina, C.R., Helffrich, G., 1994. Phase transition Clapeyron slopes and transition zone seismic discontinuity topography. *J. Geophys. Res.* 99, 15853–15860.
- Bina, C.R., Liu, M., 1995. A note on the sensitivity of mantle convection models to composition-dependent phase relations. *Geophys. Res. Lett.* 22, 2565–2568.
- Bock, G., Kind, R., 1991. A global study of S-to-P and P-to-S conversions from the upper mantle transition zone. *Geophys. J. Int.* 107, 117–129.
- Bouhifd, M.A., Andraut, D., Fiquet, G., Richet, P., 1996. Thermal expansion of forsterite up to the melting point. *Geophys. Res. Lett.* 23, 1143–1146.
- Brown, J.M., Shankland, T.J., 1981. Thermodynamic parameters in the Earth as determined from seismic profiles. *Geophys. J. R. Astr. Soc.* 66, 579–596.
- Butler, R., Anderson, D.L., 1978. Equation of state fits to the lower mantle and outer core. *Phys. Earth Planet. Int.* 17, 147–162.
- Chai, M., Michael Brown, J., Slutsky, L.J., 1997. The elastic constants of an aluminous orthopyroxene to 12.5 GPa. *J. Geophys. Res.* 102, 14779–14785.
- Chen, G., Spetzler, H.A., Getting, I.C., Yoneda, A., 1996. Selected elastic moduli and their temperature derivatives for olivine and garnet with different  $\text{Mg}/(\text{Mg} + \text{Fe})$  contents: results from GHz ultrasonic interferometry. *Geophys. Res. Lett.* 23, 5–8.
- Chen, G., Miletich, R., Mueller, K., Spetzler, H.A., 1997. Shear and compressional mode measurements with GHz ultrasonic interferometry and velocity-composition systematics for the pyrope-almandine solid solution series. *Phys. Earth Planet. Int.* 99, 273–287.
- Chopelas, A., Boehler, R., 1989. Thermal expansion measurements at very high pressure, systematics, and a case for a chemically homogeneous mantle. *Geophys. Res. Lett.* 16, 1347–1350.
- Chopelas, A., Boehler, R., 1992. Thermal expansivity in the lower mantle. *Geophys. Res. Lett.* 19, 1983–1986.
- Chopelas, A., Boehler, R., Ko, T., 1994. Thermodynamics and behaviour of  $\gamma\text{-Mg}_2\text{SiO}_4$  at high pressure: implications for  $\text{Mg}_2\text{SiO}_4$  phase equilibrium. *Phys. Chem. Miner.* 21, 351–359.
- Davaille, A., Jaupart, C., 1994. Onset of thermal convection in fluids with temperature-dependent viscosity: application to the oceanic mantle. *J. Geophys. Res.* 99, 19853–19866.
- Davies, G.F., Dziewonski, A.M., 1975. Homogeneity and constitution of the Earth's lower mantle and outer core. *Phys. Earth Planet. Int.* 10, 336–343.
- Duffy, T.S., Anderson, D.L., 1989. Seismic velocities in mantle minerals and the mineralogy of the upper mantle. *J. Geophys. Res.* 94, 1895–1912.
- Duffy, T.S., Ahrens, T.J., 1995. Compressional sound velocity, equation of state and constitutive response of shock-compressed magnesium oxide. *J. Geophys. Res.* 100, 529–542.
- Duffy, T.S., Zha, C.S., Downs, R.T., Mao, H.K., Hemley, R.J., 1995. Elasticity of forsterite to 16 GPa and the composition of the upper mantle. *Nature* 378, 170–173.
- Dziewonski, A.M., Anderson, D.L., 1981. Preliminary reference Earth model. *Phys. Earth Planet. Int.* 25, 297–356.
- Estabrook, C.H., Kind, R., 1996. The nature of the 660 km upper mantle seismic discontinuity from precursors to PP. *Science*, in press.
- Fei, Y., Saxena, S.K., Navrotsky, A., 1990. Internally consistent thermodynamic data and equilibrium phase relations for compounds in the system  $\text{MgO}$ – $\text{SiO}_2$  at high pressure and high temperature. *J. Geophys. Res.* 95, 6915–6928.
- Fei, Y., Mao, H.K., Shu, J., Hu, J., 1992a.  $P$ – $V$ – $T$  equation of state of Magnesio-wüstite ( $\text{Mg}_{0.6}\text{Fe}_{0.4}\text{O}$ ). *Phys. Chem. Miner.* 18, 416–422.
- Fei, Y., Mao, H.K., Shu, J., Parthasarathy, G., Basset, W.A., Ko, J., 1992b. Simultaneous high-P, high-T X-ray diffraction study of  $\beta\text{-(Mg,Fe)}_2\text{SiO}_4$  to 26 GPa and 900 K. *J. Geophys. Res.* 97, 4489–4495.
- Fukao, Y., Obayashi, M., Inoue, H., Nenbai, M., 1992. Subducting slabs stagnant in the mantle transition zone. *J. Geophys. Res.* 97, 4809–4822.
- Funamori, N., Yagi, T., Utsumi, W., Kondo, T., Uchida, T., Funamori, M., 1996. Thermoelastic properties of  $\text{MgSiO}_3$  perovskite determined by in situ X-ray observations up to 30 GPa and 2000 K. *J. Geophys. Res.* 101, 8257–8269.
- Gasparik, T., 1989. Transformations of enstatite–jadeite–diopside pyroxenes to garnet. *Contrib. Miner. Pet.* 102, 389–405.

- Gillet, P., Richet, P., Guyot, F., Fiquet, G., 1991. High-temperature thermodynamic properties of forsterite. *J. Geophys. Res.* 96, 11805–11816.
- Grand, S.P., Helmberger, D.V., 1984. Upper mantle shear structure of North America. *Geophys. J. R. Astr. Soc.* 76, 399–438.
- Guyot, F., Wang, Y., Gillet, P., Ricard, Y., 1996. Quasi-harmonic computations of thermodynamic parameters of olivines at high-pressure and high-temperature. A comparison with experiment data. *Phys. Earth Planet. Int.* 98, 17–29.
- Hazen, R.M., Downs, R.T., Conrad, P.G., Finger, L.W., Gasparik, T., 1994. Comparative compressibilities of majorite-type garnets. *Phys. Chem. Miner.* 21, 344–349.
- Hugh-Jones, D.A., Angel, R.J., 1997. Effect of  $\text{Ca}^{2+}$  and  $\text{Fe}^{2+}$  on the equation of state of  $\text{MgSiO}_3$  orthopyroxene. *J. Geophys. Res.* 102, 12333–12340.
- Irifune, T., 1987. An experimental investigation of the pyroxene-garnet transformation in a pyrolite composition and its bearing on the constitution of the mantle. *Phys. Earth Planet. Int.* 45, 324–336.
- Irifune, T., 1994. Absence of an aluminous phase in the upper part of the Earth's lower mantle. *Nature* 370, 131–133.
- Irifune, T., Ringwood, A.E., 1987. Phase transformations in a harzburgite composition to 26 GPa: implications for dynamical behaviour of subducted slabs. *Earth Planet. Sci. Lett.* 86, 365–376.
- Irifune, T., Koizumi, T., Ando, J.I., 1996. An experimental study of the garnet-perovskite transformation in the system  $\text{MgSiO}_3$ – $\text{Mg}_3\text{Al}_2\text{Si}_3\text{O}_{12}$ . *Phys. Earth Planet. Int.* 96, 147–157.
- Isaak, D.G., 1992. High temperature elasticity of iron-bearing olivines. *J. Geophys. Res.* 97, 1871–1885.
- Isaak, D.G., Anderson, O.L., Oda, H., 1992. High temperature thermal expansion and elasticity of calcium-rich garnet. *Phys. Chem. Miner.* 19, 106–120.
- Ita, J., Stixrude, L., 1992. Petrology, elasticity and composition of the mantle transition zone. *J. Geophys. Res.* 97, 6849–6866.
- Ita, J., Stixrude, L., 1993. Density and elasticity of model upper mantle compositions and their implications for whole mantle structure. In: Takahashi, E., Jeanloz, R., Rubie, D.C. (Eds.), *Evolution of the Earth and Planets*, *Geophys. Monogr.* 74, IUGG vol. 14, pp. 111–130.
- Ito, E., Navrotsky, A., 1985.  $\text{MgSiO}_3$  ilmenite: calorimetry, phase equilibria and decomposition at room pressure. *Am. Mineral.* 70, 1020–1026.
- Ito, E., Takahashi, E., 1989. Post-spinel transformations in the system  $\text{Mg}_2\text{SiO}_4$ – $\text{Fe}_2\text{SiO}_4$  and some geophysical implications. *J. Geophys. Res.* 94, 10637–10646.
- Jackson, I., Ridgen, S.M., 1996. Analysis of  $P$ – $V$ – $T$  data: constraints on the thermoelastic properties of high-pressure minerals. *Phys. Earth Planet. Int.* 96, 85–112.
- Jeanloz, R., Thompson, A.B., 1983. Phase transitions and mantle discontinuities. *Rev. Geophys. Space Phys.* 21, 51–74.
- Jeanloz, R., Morris, S., 1986. Temperature distribution in the crust and mantle. *Annu. Rev. Earth Planet. Sci.* 14, 337–415.
- Kajiyoshi, K., 1986. High-temperature equation of state for mantle minerals and their anharmonic properties, PhD Thesis, Okayama University, Japan.
- Kandelin, J., Weidner, D.J., 1988. The single-crystal elastic properties of jadeite. *Phys. Earth Planet. Int.* 50, 251–260.
- Kanzaki, M., 1987. Ultrahigh-pressure phase relations in the system  $\text{Mg}_4\text{Si}_4\text{O}_{12}$ – $\text{Mg}_3\text{Al}_2\text{Si}_3\text{O}_{12}$ . *Phys. Earth Planet. Int.* 49, 168–175.
- Kato, T., Ohtani, E., Morishima, H., Yamazaki, D., Suzuki, A., Suto, M., Kubo, T., Kikegawa, T., Shimomura, O., 1995. In situ X-ray observation of high-pressure phase transitions of  $\text{MgSiO}_3$  and thermal expansion of  $\text{MgSiO}_3$  perovskite at 25 GPa by double-stage multianvil system. *J. Geophys. Res.* 100, 20475–20481.
- Katsura, T., Ito, E., 1989. The system  $\text{Mg}_2\text{SiO}_4$ – $\text{Fe}_2\text{SiO}_4$  at high pressures and temperatures: precise determination of stabilities of olivine, modified spinel and spinel. *J. Geophys. Res.* 94, 15663–15670.
- Katsura, T., Ito, E., 1996. Determination of Fe–Mg partitioning between perovskite and magnesiowüstite. *Geophys. Res. Lett.* 23, 2005–2008.
- Kennett, B.L.N., 1991. Seismic velocity gradients in the upper mantle. *Geophys. Res. Lett.* 18, 1115–1118.
- Kennett, B.L.N., Engdahl, E.R., Buland, R., 1995. Constraints on seismic velocities in the Earth from travel times. *Geophys. J. Int.* 122, 108–124.
- Lefevre, L.V., Helmberger, D.V., 1989. Upper mantle P velocity structure of the Canadian shield. *J. Geophys. Res.* 94, 17749–17765.
- Li, B., Gwanmesia, G.D., Liebermann, R.C., 1996. Sound velocities of olivine and beta polymorphs of  $\text{Mg}_2\text{SiO}_4$  at Earth's transition zone pressures. *Geophys. Res. Lett.* 23, 2259–2262.
- Liu, M., 1994. Asymmetric phase effects and mantle convection patterns. *Science* 264, 1904–1907.
- Lu, R., Hofmeister, A.M., Wang, Y., 1994. Thermodynamic properties of ferromagnesian silicate perovskites from vibrational spectroscopy. *J. Geophys. Res.* 99, 11795–11804.
- Machetel, P., Weber, P., 1991. Intermittent layered convection in a model mantle with an endothermic phase change at 670 km. *Nature* 350, 55–57.
- Mao, H.K., Hemley, R.J., Fei, Y., Shu, J.F., Shen, L.C., Jephcoat, A.P., Wu, Y., Bassett, W.A., 1991. Effect of pressure, temperature and composition on lattice parameters and density of  $(\text{Fe,Mg})\text{SiO}_3$ -perovskites to 30 GPa. *J. Geophys. Res.* 96, 8069–8080.
- Martinez, I., Wang, Y., Guyot, F., Liebermann, R.C., Doukhan, J.-C., 1997. Microstructures and iron partitioning in  $(\text{Mg,Fe})\text{SiO}_3$  perovskite– $(\text{Mg,Fe})\text{O}$  magnesiowüstite assemblages: an analytical transmission electron microscopy study. *J. Geophys. Res.* 102, 5265–5280.
- Meng, Y., Weidner, D.J., Gwanmesia, G.D., Liebermann, R.C., Vaughan, M.T., Wang, Y., Leinenweber, K., Pacalo, R.E., Yeganeh-Haeri, A., Zhao, Y., 1993. In situ high  $P$ – $T$  X-ray diffraction studies on three polymorphs ( $\alpha, \beta, \gamma$ ) of  $\text{Mg}_2\text{SiO}_4$ . *J. Geophys. Res.* 98, 22199–22207.
- Meng, Y., Fei, Y., Weidner, D.J., Gwanmesia, G.D., Hu, J., 1994. Hydrostatic compression of  $\gamma$ - $\text{Mg}_2\text{SiO}_4$  to mantle pressures and 700 K: thermal equation of state and related thermoelastic properties. *Phys. Chem. Miner.* 21, 407–412.
- Montagner, J.P., Kennett, B.L.N., 1996. How to reconcile body-

- wave and normal mode reference Earth models. *Geophys. J. Int.* 125, 229–248.
- Niu, F., Kawakatsu, H., 1996. Complex structure of the mantle discontinuities at the tip of the subducting slab beneath the Northeast China: a preliminary investigation of broadband receiver functions. *J. Phys. Earth* 44, 701–711.
- O'Neil, B., Jeanloz, R., 1994.  $\text{MgSiO}_3$ – $\text{FeSiO}_3$ – $\text{Al}_2\text{O}_3$  in the Earth's lower mantle: perovskite and garnet at 1200 km depth. *J. Geophys. Res.* 99, 19901–19915.
- Pacalo, R.E.G., Weidner, D.J., 1997. Elasticity of majorite,  $\text{MgSiO}_3$  tetragonal garnet. *Phys. Earth Planet. Int.* 99, 145–154.
- Pacalo, R.E.G., Weidner, D.J., Gasparik, T., 1992. Elastic properties of sodium rich majorite garnet. *Geophys. Res. Lett.* 19, 1895–1898.
- Paulssen, H., 1988. Evidence for a sharp 670 km discontinuity as inferred from P-to-S converted waves. *J. Geophys. Res.* 93, 10489–10500.
- Peltier, W.R., Solheim, L.P., 1992. Mantle phase transitions and layered chaotic convection. *Geophys. Res. Lett.* 19, 321–324.
- Plymate, T.G., Stout, J.H., 1994. Pressure–Volume–Temperature behaviour of  $\gamma\text{-Fe}_2\text{SiO}_4$  (spinel) based on static compression measurements at 400°C. *Phys. Chem. Miner.* 21, 413–420.
- Poirier, J.P., 1991. *Introduction to the Physics of the Earth's Interior*. Cambridge Univ. Press, Cambridge, UK, 264 pp.
- Revenaugh, J., Jordan, T.H., 1991. Mantle layering from ScS reverberations: 2. The transition zone. *J. Geophys. Res.* 96, 19763–19780.
- Revenaugh, J., Sipkin, S.A., 1994. Mantle discontinuity structure beneath China. *J. Geophys. Res.* 99, 21911–21927.
- Reynard, B., Guyot, F., 1994. High-temperature properties of Geikielite ( $\text{MgTiO}_3$ –ilmenite) from high temperature high pressure Raman spectroscopy—some implications for  $\text{MgSiO}_3$  ilmenite. *Phys. Chem. Miner.* 21, 441–450.
- Reynard, B., Rubie, D.C., 1996. High-pressure, high-temperature Raman spectroscopic study of ilmenite-type  $\text{MgSiO}_3$ . *Am. Mineral.* 81, 1092–1096.
- Reynard, B., Fiquet, G., Itié, J.P., Rubie, D.C., 1996. High-pressure X-ray diffraction study and equation of state of  $\text{MgSiO}_3$  ilmenite. *Am. Mineral.* 81, 45–50.
- Ridgen, S.M., Gwanmesia, G.D., FitzGerald, J.D., Jackson, I., Liebermann, R.C., 1991. Spinel elasticity and seismic structure of the transition zone of the mantle. *Nature* 354, 143–145.
- Ridgen, S.M., Gwanmesia, G.D., Liebermann, R.C., 1994. Elastic wave velocities of a pyrope-majorite garnet to 3 GPa. *Phys. Earth Planet. Int.* 86, 35–44.
- Ringwood, A.E., 1975. *Composition and petrology of the Earth's mantle*, McGraw-Hill, New-York, 678 pp.
- Sammis, C., Anderson, D.L., Jordan, T., 1970. Application of isotropic finite strain theory to ultrasonic and seismological data. *J. Geophys. Res.* 75, 4478–4480.
- Sawamoto, H., 1987. Phase diagram of  $\text{MgSiO}_3$  at pressures up to 24 GPa and temperatures up to 2200 K: phase stability and properties of tetragonal garnet. In: Manghani, M.H., Syono, Y. (Eds.), *High Pressure Research in Mineral Physics*. Am. Geophys. Union, *Geophys. Monogr. Ser.* 39, 209–219.
- Saxena, S.K., Shen, G., 1992. Assessed data on heat capacity, thermal expansion and compressibility for some oxides and silicates. *J. Geophys. Res.* 97, 19813–19825.
- Saxena, S.K., Chatterjee, N., Fei, Y., Shen, G., 1993. *Thermodynamic Data on Oxides and Silicates*. Springer, Berlin.
- Schimmel, M., 1997. Distinct body wave phenomena caused by mantle structure. PhD Thesis, Utrecht University, 101 pp.
- Shearer, P.M., 1993. Global mapping of upper mantle reflectors from long period SS precursors. *Geophys. J. Int.* 115, 878–904.
- Shearer, P.M., 1996. Transition zone velocity gradients and the 520 km depth discontinuity. *J. Geophys. Res.* 101, 3053–3066.
- Sinogeikin, S.V., Bass, J.D., O'Neil, B., Gasparik, T., 1997. Elasticity of tetragonal end-member majorite and solid solutions in the system  $\text{Mg}_4\text{Si}_4\text{O}_{12}$ – $\text{Mg}_3\text{Al}_2\text{Si}_3\text{O}_{12}$ . *Phys. Chem. Miner.* 24, 115–121.
- Skinner, B.J., 1966. Thermal expansion. In: Clark Jr., S.P. (Ed.), *Handbook of Physical Constants*. Geol. Soc. Am. Memoir 97, pp. 75–96.
- Sotin, C., Parmentier, E.M., 1989. On the stability of a fluid layer containing a univariant phase transition: application to planetary interiors. *Phys. Earth Planet. Int.* 55, 10–25.
- Sotin, C., Labrosse, S., 1997. Thermal convection in an isoviscous infinite Prandtl number fluid heated from within and from below: applications to the transfert of heat through planetary mantles. Submitted to *Phys. Earth Planet. Int.*
- Stixrude, L., Bukowski, M.S.T., 1990. Fundamental thermodynamic relations and silicate melting with implications for the constitution of D". *J. Geophys. Res.* 95, 19311–19325.
- Stixrude, L., Hemley, R.J., Fei, Y., Mao, H.K., 1992. Thermoelasticity of silicate perovskite and magnesio-wüstite of the Earth's mantle. *Science* 257, 1099–1101.
- Sumino, Y., Anderson, O.L., 1984. Elastic constants of minerals. In: Carmichael, R.S. (Ed.), *Handbook of Physical Properties of Rocks*. CRC Press, Boca Raton, FL, III, 39–137.
- Suzuki, I., Takei, H., Anderson, O.L., 1984. Thermal expansion of forsterite,  $\text{Mg}_2\text{SiO}_4$ . In: Hahn, T.A. (Ed.), *Thermal expansion* 8. Plenum Publ., pp. 79–88.
- Tackley, P.J., 1993. Effect of strongly temperature-dependent viscosity on time-dependent, three-dimensional models of mantle convection. *Geophys. Res. Lett.* 20, 2187–2190.
- Tackley, P.J., Stevenson, D.J., Glatzmaier, G.A., Schubert, G., 1994. Effects of multiple phase transitions in a three-dimensional spherical model of convection in Earth's mantle. *J. Geophys. Res.* 99, 15877–15901.
- Takahashi, E., Ito, E., 1987. Mineralogy of mantle peridotite along a model geotherm up to 700 km depth. In: Manghani, M.H., Syono, Y. (Eds.), *High pressure research in mineral physics*. Am. Geophys. Union, *Geophys. Monogr. Ser.* 39, 427–437.
- Turcotte, D.L., Schubert, G., 1982. *Geodynamics*, Wiley, New York, NY, 450 pp.
- Utsumi, W., Funamori, N., Yagi, T., Ito, E., Kikegawa, T., Shimomura, O., 1995. Thermal expansivity of  $\text{MgSiO}_3$  perovskite under high pressures up to 20 GPa. *Geophys. Res. Lett.* 22, 1005–1008.
- Vacher, P., Mocquet, A., Sotin, C., 1996. Comparison between tomographic structures and models of convection in the upper mantle. *Geophys. J. Int.* 124, 45–56.

- Verhoogen, J., 1965. Phase changes and convection in the Earth's mantle. *Phil. Trans. R. Soc. London, Ser. A* 258, 276–283.
- Vidale, J.E., Benz, H.M., 1992. Upper mantle seismic discontinuities and the thermal structure of subduction zones. *Nature* 356, 678–683.
- Vidale, J.E., Ding, X.Y., Grand, S.P., 1995. The 410-km depth discontinuity: a sharpness estimate from near critical reflections. *Geophys. Res. Lett.* 22, 2557–2560.
- Wang, Y., Weidner, D.J., Liebermann, R.C., Zhao, Y., 1994.  $P$ – $V$ – $T$  equation of state of (Mg,Fe)SiO<sub>3</sub> perovskite: constraints on composition of the lower mantle. *Phys. Earth Planet. Int.* 83, 13–40.
- Wang, Y., Weidner, D.J., Guyot, F., 1996. Thermal equation of state of CaSiO<sub>3</sub> perovskite. *J. Geophys. Res.* 101, 661–672.
- Webb, S.L., Jackson, I., 1993. The pressure dependence of the elastic moduli of single-crystal orthopyroxene (Mg<sub>0.8</sub>Fe<sub>0.2</sub>)SiO<sub>3</sub>. *Eur. J. Mineral.* 5, 1111–1119.
- Weidner, D.J., Ito, E., 1985. Elasticity of MgSiO<sub>3</sub> in the ilmenite phase. *Phys. Earth Planet. Int.* 40, 65–70.
- Weidner, D.J., Sawamoto, H., Sasaki, S., Kumazawa, M., 1984. Single-crystal elastic properties of the spinel phase of Mg<sub>2</sub>SiO<sub>4</sub>. *J. Geophys. Res.* 89, 7852–7860.
- Weidner, D.J., Wang, Y., Yeganeh-Haeri, A., 1993. Equation of state properties of mantle perovskites. *EOS Trans. AGU* 74, 571.
- Wicks, C.W., Richards, M.A., 1993. A detailed map of the 660-km discontinuity beneath the Izu–Bonin subduction zone. *Science* 261, 1424–1427.
- Wolf, G.H., Jeanloz, R., 1985. Lattice dynamics and structural distortions of CaSiO<sub>3</sub> and MgSiO<sub>3</sub> perovskites. *Geophys. Res. Lett.* 12, 413–416.
- Wood, B.J., Rubie, D.C., 1996. The effect of alumina on phase transformations at the 660-km discontinuity from Fe–Mg partitioning experiments. *Science* 273, 1522–1524.
- Woodland, A.B., Angel, R.J., 1997. Reversal of the orthoferrosilite–high- $P$  clinoferrosilite transition, a phase diagram for FeSiO<sub>3</sub> and implications for the mineralogy of the Earth's upper mantle. *Eur. J. Mineral.* 9, 245–254.
- Yagi, T., Bell, P.M., Mao, H.K., 1979. Phase relations in the system MgO–FeO–SiO<sub>2</sub> between 150 and 700 kbar at 1000°C. *Carnegie Inst. Washington Year Book* 78, 614–618.
- Yamazaki, A., Hirahara, K., 1994. The thickness of upper mantle discontinuities, as inferred from short period J-array data. *Geophys. Res. Lett.* 21, 1811–1814.
- Yeganeh-Haeri, A., 1994. Synthesis and re-investigation of the elastic properties of single crystal magnesium silicate perovskite. *Phys. Earth Planet. Int.* 87, 111–121.
- Yeganeh-Haeri, A., Weidner, D.J., Ito, E., 1989. Single-crystal elastic modulus of magnesium metasilicate perovskite. *Geophys. Monogr. Am. Geophys. Union* 45, 13–35.
- Yusa, H., Akaogi, M., Ito, E., 1993. Calorimetric study of MgSiO<sub>3</sub> garnet and pyroxene: heat capacities, transition enthalpies and equilibrium phase relations in MgSiO<sub>3</sub> at high pressures and temperatures. *J. Geophys. Res.* 98, 6453–6460.
- Zaug, J.M., Abramson, E.H., Brown, J.M., Slutsky, L.J., 1993. Sound velocities in Olivine at Earth mantle pressures. *Science* 260, 1487–1489.
- Zha, C.S., Duffy, T.S., Downs, R.T., Mao, H.K., Hemley, R.J., 1996. Sound velocity and elasticity of single-crystal forsterite to 16 GPa. *J. Geophys. Res.* 101, 17535–17545.
- Zha, C.S., Duffy, T.S., Mao, H.K., Downs, R.T., Hemley, R.J., Weidner, D.J., 1997. Single-crystal elasticity of  $\beta$ -Mg<sub>2</sub>SiO<sub>4</sub> to the pressure of the 410 km seismic discontinuity in the Earth's mantle. *Earth Planet. Sci. Lett.* 147, E9–E15.
- Zhang, L., Ahsbahs, H., Hafner, S.S., Kutoglu, A., 1997. Single-crystal compression and crystal structure of clinopyroxene up to 10 GPa. *Am. Mineral.* 82, 245–258.
- Zhao, Y., Anderson, D.L., 1994. Mineral physics constraints on the chemical composition of the Earth's lower mantle. *Phys. Earth Planet. Int.* 85, 273–292.
- Zhao, Y., Schiferl, D., Shankland, T.J., 1995. A high  $P$ – $T$  single-crystal X-ray diffraction study of thermoelasticity of MgSiO<sub>3</sub> orthoenstatite. *Phys. Chem. Miner.* 22, 393–398.
- Zhao, Y., Von Dreele, R.B., Shankland, T.J., Weidner, D.J., Zhang, J., Wang, Y., Gasparik, T., 1997. Thermoelastic equation of state of jadeite NaAlSi<sub>2</sub>O<sub>6</sub>: an energy dispersive Reitveld refinement study of low symmetry and multiple phases diffraction. *Geophys. Res. Lett.* 24, 5–8.